The SCUBA HAlf Degree Extragalactic Survey — III. Identification of radio and mid-infrared counterparts to submillimetre galaxies

R. J. Ivison,[1,2] T. R. Greve,[3] J. S. Dunlop,[2] J. A. Peacock,[2] E. Egami,[4] Ian Smail,[5] E. Ibar,[2] E. van Kampen,[6] I. Aretxaga,[7] T. Babbedge,[8] A. D. Biggs,[1] A. W. Blain,[3] S. C. Chapman,[9] D. L. Clements,[8] K. Coppin,[5,10] D. Farrah,[11] M. Halpern,[10] D. H. Hughes,[7] M. J. Jarvis,[12] T. Jenness,[13] J. R. Jones,[14] A. M. J. Mortier,[2] S. Oliver,[15] C. Papovich,[4] P. G. Pérez-González,[16] A. Pope,[10] S. Rawlings,[17] G. H. Rieke,[4] M. Rowan-Robinson,[8] R. S. Savage,[15] D. Scott,[10] M. Seigar,[18] S. Serjeant,[19] C. Simpson,[20] J. A. Stevens,[12] M. Vaccari,[21,8] J. Wagg[7,22] and C. J. Willott[23]

[1] UK Astronomy Technology Centre, Royal Observatory, Blackford Hill, Edinburgh EH9 3HJ
[2] Scottish Universities Physics Alliance, Institute for Astronomy, University of Edinburgh, Blackford Hill, Edinburgh EH9 3HJ
[3] Astronomy Department, California Institute of Technology, Pasadena, CA 91125, USA
[4] Steward Observatory, University of Arizona, 933 N. Cherry Avenue, Tuscon, AZ 85721, USA
[5] Institute for Computational Cosmology, University of Durham, South Road, Durham DH1 3LE
[6] Institute for Astrophysics, University of Innsbruck, Technikerstr. 25, A-6020 Innsbruck, Austria
[7] Instituto Nacional de Astrofísica, Optica y Electrónica, Apartado Postal 51 y 216, 72000 Puebla, Pue., Mexico
[8] Astrophysics Group, Blackett Laboratory, Imperial College London, Prince Consort Road, London SW7 2BW
[9] Institute of Astronomy, Madingley Road, Cambridge, CB3 0HA
[10] Department of Physics & Astronomy, University of British Columbia, Vancouver, BC V6T 1Z1, Canada
[11] Department of Astronomy, Cornell University, 106 Space Sciences, Ithaca, NY 14853, USA
[12] Centre for Astrophysics Research, University of Hertfordshire, College Lane, Hatfield AL10 9AB
[13] Joint Astronomy Centre, 660 N. A'ohōkū Place, University Park, Hilo, HI 96720, USA
[14] Center for Astrophysics and Space Astronomy, 389 UCB, Boulder, CO 80309, USA
[15] Astronomy Centre, University of Sussex, Falmer, Brighton BN1 9QH
[16] Departmento de Astrofísica y CC. de Atmósfera, Facultad de CC. Físicas, Universidad Complutense de Madrid, 28040 Madrid, Spain
[17] Astrophysics, Department of Physics, Denys Wilkinson Building, Keble Road, Oxford OX1 3RH
[18] Department of Physics and Astronomy, 4129 Frederick Reines Hall, University of California, Irvine, CA 92697, USA
[19] Astrophysics Group, Department of Physics, The Open University, Milton Keynes MK7 6AA
[20] Astrophysics Research Institute, Liverpool John Moores University, Twelve Quays House, Egerton Wharf, Birkenhead CH41 1LD
[21] Department of Astronomy, University of Padova, Vicolo dell'Osservatorio 3, I-35122, Italy
[22] National Radio Astronomy Observatory, P.O. Box 0, Socorro, NM 87801, USA
[23] Physics Department, University of Ottawa, 150 Louis Pasteur, Pavillon MacDonald Hall, Ottawa, Ontario K1N 6N5, Canada

arXiv:astro-ph/0702544v2 30 May 2007

ABSTRACT

Determining an accurate position for a submillimetre (submm) galaxy (SMG) is the crucial step that enables us to move from the basic properties of an SMG sample – source counts and 2-D clustering – to an assessment of their detailed, multi-wavelength properties, their contribution to the history of cosmic star formation and their links with present-day galaxy populations. In this paper, we identify robust radio and/or infrared (IR) counterparts, and hence accurate positions, for over two thirds of the SCUBA HAlf-Degree Extragalactic Survey (SHADES) Source Catalogue, presenting optical, 24-μm and radio images of each SMG. Observed trends in identification rate have given no strong rationale for pruning the sample. Uncertainties in submm position are found to be consistent with theoretical expectations, with no evidence for significant additional sources of error. Employing the submm/radio redshift indicator, via a parameterisation appropriate for radio-identified SMGs with spectroscopic redshifts, yields a median redshift of 2.8 for the radio-identified subset of SHADES, somewhat higher than the median spectroscopic redshift. We present a diagnostic colour-colour plot, exploiting *Spitzer* photometry, in which we identify regions commensurate with SMGs at very high redshift. Finally, we find that significantly more SMGs have multiple robust counterparts than would be expected by chance, indicative of physical associations. These multiple systems are most common amongst the brightest SMGs and are typically separated by 2–6 arcsec, ~15–50/sin i kpc at $z \sim 2$, consistent with early bursts seen in merger simulations.

Key words: galaxies: starburst – galaxies: formation – cosmology: observations – cosmology: early Universe

1   INTRODUCTION

Observational cosmology in the submm waveband has been one of the few fields that can claim to have beaten Moore's Law (Moore 1965), the other notable astronomical exception being the Virgo consortium's 'Millennium Simulation' (Springel et al. 2005). It has benefited enormously from the development of bolometer arrays such as SCUBA (Holland et al. 1999) and MAMBO (Kreysa et al. 1998): the commissioning of these groundbreaking cameras, on the James Clerk Maxwell Telescope (JCMT) and the IRAM 30-m telescope, respectively, yielded a thousand-fold increase in mapping speed over single-pixel devices such as UKT14 (Duncan et al. 1990). A decade on, the next generation of cameras exemplified by LABOCA (Kreysa et al. 2003) and SCUBA-2 (Holland et al. 2003) will yield a similar increase in mapping speed over existing arrays.

SCUBA brought about a radical shift in our understanding of the formation and evolution of galaxies, with the discovery that luminous, dusty galaxies were a thousand times more abundant in the early Universe than at the present day (Smail, Ivison & Blain 1997; Hughes et al. 1998; Barger et al. 1998; Eales et al. 1999). SCUBA was capable of providing only approximate coordinates so it was immediately clear that the nature of these sources would remain a mystery until more accurate positions could be determined – the subject of this paper. To refine positions provided by SCUBA, we are reliant on radio observations; the radio emission is a high-resolution proxy for the rest-frame far-IR emission observed in the submm (Ivison et al. 1998, 2000, 2002; Smail et al. 2000; Webb et al. 2003a; Clements et al. 2004; Dannerbauer et al. 2004; Borys et al. 2004; Garrett, Knudsen & van der Werf 2005; Voss et al. 2006). Although likely to be inefficient in the era of SCUBA-2, radio imaging also enabled large samples of SMGs to be acquired by targeting optically faint μJy radio sources (OFRS) using SCUBA's fast PHOTOM mode (Barger, Cowie & Richards 1999; Chapman et al. 2002).

Mid-IR imaging with *Spitzer* has also proved useful for refining SMG positions (Egami et al. 2004; Ivison et al. 2004; Pope et al. 2006; Ashby et al. 2006), albeit with poor angular resolution and an imprecise connection to bolometric luminosity. To be useful, such data need to be close to the 24-μm confusion limit ($\sim$50 μJy), so radio imaging is likely to remain the preferred procedure.

Radio and submm flux densities, taken together, are sensitive to redshift (Carilli & Yun 1999; Dunne, Clements & Eales 2000; Rengarajan & Takeuchi 2001), albeit limited to $z \lesssim 3$ by the depth of radio imaging available currently. This approach is the subject of paper IV in this series (Aretxaga et al. 2007). Early work in this vein constrained the median redshift of the SMG population to be $z \gtrsim 2$ (Carilli & Yun 2000; Smail et al. 2000; Ivison et al. 2002).

The true triumph of the radio identification procedure, however, has been in identifying the correct optical/IR counterparts so that their morphologies, colours, magnitudes, etc. can be determined unambiguously; more importantly, this has also allowed spectroscopists to place their slits accurately, sometimes on apparently blank sky when optical counterparts were too faint for existing imaging ($R_{AB} \gtrsim 26$, e.g. LE850.12 and SSA13.332 – Chapman et al. 2005). This painstaking approach was slow to pay dividends, with only a handful of redshifts reported initially (Ivison et al. 1998, 2000; Barger et al. 1999; Ledlow et al. 2002; Knudsen, van der Werf & Jaffe 2003; Simpson et al. 2004). Deeper radio observations allied with the largest existing submm surveys and the OFRS technique resulted eventually in the acquisition of approximately 100 spectroscopic redshifts, the majority by Chapman et al. (2003, 2005). This has enabled the direct detection of colossal
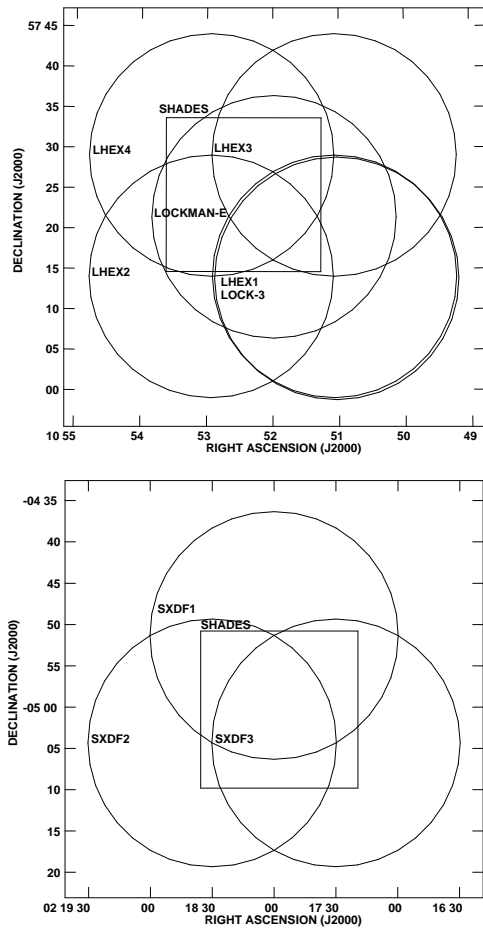
molecular gas reservoirs in a representative sample of SMGs (Neri et al. 2003; Greve et al. 2005; Tacconi et al. 2006), following on from the pioneering CO detections of Frayer et al. (1998, 1999). It allowed Alexander et al. (2005a, 2005b) to suggest that the bulk of the SMG population contains obscured, often Compton-thick, active galactic nuclei (AGN) via the first meaningful analysis of their X-ray properties; it permitted a rigorous test of the radio/far-IR relation at high redshift, via observations near the peak of SMG spectral energy distributions (SEDs) at 350 μm (Kovacs et al. 2006) and, finally, it allowed a thorough analysis of their rest-frame optical photometric and spectroscopic properties (Smail et al. 2004; Swinbank et al. 2004; Takata et al. 2006).

Until now, the most adventurous blank-field surveys have covered a few $\times 100$ arcmin^2, detecting typically 40 galaxies (Scott et al. 2002; Webb et al. 2003a; Borys et al. 2003; Greve et al. 2004). The properties of these galaxies were quickly characterised over the entire observable spectral range (Lilly et al. 1999; Eales et al. 2000; Gear et al. 2000; Lutz et al. 2001; Fox et al. 2002; Ivison et al. 2002; Webb et al. 2003a, 2003b; Waskett et al. 2003; Borys et al. 2004; Dunlop et al. 2004; Pope et al. 2005, 2006), but it soon became clear that some of the key remaining questions – the degree of clustering and the role played by AGN – could only be addressed by a significantly larger sample selected homogeneously from contiguous sky.

Despite the steep slope of the submm number counts (Blain et al. 1998, 1999), the 850-μm confusion limit – set at around 2 mJy by the JCMT's 15-m primary – dictates that we must map more sky if we are to obtain larger samples with well-characterised positions and flux densities. SHADES aimed to detect 200 SMGs over two 0.25-degree^2 fields – the Lockman Hole (LH; 10h 52m, $+57°.4$) and the Subaru-*XMM-Newton* Deep Field (SXDF; 02h 18m, $-5°.0$). See Mortier et al. (2005), Paper I of this series, for a description of its motivation and design. SCUBA was retired in 2005 July, before SHADES could be completed, after two years plagued by cryogenic problems. The SHADES Source Catalogue, gleaned from 800 arcmin^2 and comprising 120 SMGs in the LH and the SXDF, is presented in Paper II of this series (Coppin et al. 2006).

In this, Paper III, we identify radio and/or mid-IR counterparts and hence accurate positions for the SHADES sample using 1.4-GHz radio imaging from the National Radio Astronomy Observatory's (NRAO[1]) Very Large Array (VLA) and 24-μm data from MIPS (Rieke et al. 2004) on board *Spitzer* (Werner et al. 2004). This is the crucial step that allows us to move from the basic properties of an SMG sample – source counts and 2-dimensional clustering – to an assessment of their detailed properties across the entire accessible wavelength range, their contribution to the history of cosmic star formation and their links with present-day galaxy populations. In §2 we describe the data exploited in §3 to find radio and mid-IR counterparts for our SMG sample. We use these associations in §4 to determine the positional uncertainty associated with SMGs, comparing with theory developed in Appendix B. In §5 we discuss SMGs with multiple, robust counterparts and in §6 we explore identification trends. Finally, in §7 and §8 we utilise the magnitudes and colours of SMGs, now robustly identified, to constrain their redshift distribution and to identify outliers. We assume $\Omega_m = 0.27$, $\Omega_\Lambda = 0.73$, $H_0 = 71 \, \mathrm{km \, s^{-1} \, Mpc^{-1}}$ throughout (Spergel et al. 2003).

---

[1] NRAO is operated by Associated Universities Inc., under a cooperative agreement with the National Science Foundation.

ence and by a prolonged failure of the correlator, but the equivalent of around 60 hr of normal integration were salvaged. These A-configuration data were combined with the B- and C-configuration data described by Simpson et al. (2006) resulting in a 9:3:1 ratio of recorded A:B:C visibilities, evenly distributed in three pointings separated by 15 arcmin (see Fig. 1). Each pointing was imaged as a 37-piece mosaic, as with the LH. The final image was knitted together and corrected for the response of the primary beam using the AIPS task, FLATN. The resulting noise level is around $6.3 \, \mu$Jy beam^{-1} in the best regions of the map, though as high as $8.4 \, \mu$Jy beam^{-1} near bright, complex radio emitters, with a synthesised beam measuring around 1.7 arcsec (FWHM). As with the LH, we also utilise a low-resolution map, tapering our entire dataset to give a 4.2-arcsec synthesised beam.

2.2 Optical imaging

R-band optical imaging for the LH and SXDF were obtained using the Subaru 8-m telescope. The LH data were taken from the archive and are described in Ivison et al. (2004) and reach a 3σ depth of 27.7 mag; similar data for SXDF are described by Furusawa et al. (in preparation), reaching a 3σ depth of 27.5 mag (both on the Vega scale, for 2-arcsec-diameter apertures).

2.3 Near- and mid-IR imaging

The near- and mid-IR data employed here were obtained using IRAC (at 4.5 and 8 μm) and MIPS (at 24 μm). The imaging covers the entire SHADES region of the LH to near-uniform depths of $\sigma = 0.54$, 4.4 and 11 μJy at 4.5, 8 and 24 μm, respectively (Egami et al., in preparation), with flux calibration accurate to ± 10 per cent, that is approximately $3\times$ deeper at 24 μm than the data used by Egami et al. (2004), Serjeant et al. (2004) and Ivison et al. (2004). In the SXDF, IRAC and MIPS data are available from the *Spitzer* Wide-area InfraRed Extragalactic (SWIRE – Lonsdale et al. 2003) survey and reach a near-uniform depth of $\sigma = 1.1$, 7.5 and 48 μJy at 4.5, 8 and 24 μm (Shupe et al., in preparation). For comparison, the 5-σ confusion limit at 24 μm, with 20 beams per source, is around 56 μJy.

3 ASSOCIATIONS BETWEEN SUBMM GALAXIES AND RADIO/MID-IR SOURCES

Observations in the submm waveband are sensitive to cold dust created for the most part by supernovae (SNe) and stellar winds, re-radiating energy absorbed from hot, young stars (Whittet 1992). The radio waveband is also sensitive to SNe – and hence to recent star formation – via synchrotron radiation from relativistic electrons. Near-IR wavelengths probe photospheric emission from stars and in the mid-IR, at 24 μm, we are sensitive to emission from dust in the circumnuclear torus of AGN and to the warmest dust in starbursts. The correlation between submm and radio emission from SMGs is poorer than expected (from local studies – e.g. Dunne et al. 2000), probably due to a wide range of characteristic dust temperatures and to the effect of radio-loud AGN; nevertheless, predicting the rest-frame far-IR properties of SMGs is better accomplished from the radio end of the SED than from the near- or mid-IR, adding to the benefit of very high spatial resolution ($\sim$0.1 arcsec) available at radio wavelengths (Chapman et al. 2004; Muxlow et al. 2005; Biggs et al., in preparation) and making it the

Figure 1. Individual pointings for radio mosaics in the SHADES fields, together with an indication of the submm coverage. The diameter of the circles is the FWHM of the VLA's primary beam at 1.4 GHz.

2 OBSERVATIONS

2.1 1.4-GHz radio imaging

Wide-field radio images were obtained using the VLA. The LH data used here, comprising 75 hr of integration on a field designated LOCKMAN-E, were described in detail by Ivison et al. (2002). The data have since been re-analysed by Biggs & Ivison (2006), using the 37-piece mosaicing technique described by Owen et al. (2005), together with additional self-calibration. The resulting image covers most of the primary beam, out to a radius of 23 arcmin. Once combined, the noise level is unusually uniform, $4.2 \, \mu$Jy beam^{-1} r.m.s. in the centre of the field, with a 1.3-arcsec synthesised beam (FWHM).

We also utilise a new low-resolution map, made by tapering our LOCKMAN-E data to give a 4.2-arcsec synthesised beam and then mosaicing with B-configuration data taken for several nearby pointings: a new field, 11 arcmin to the south west, designated LOCK-3, plus archival data for fields designated LHEX1, LHEX2, LHEX3 and LHEX4, where LHEX4 comprises 31 hr of integration, 11 arcmin to the north east of LOCKMAN-E. Fig. 1 illustrates the mosaic of pointings. These data, together with matched-resolution 610-MHz imaging from the Giant Metre-wave Telescope in Pune, India, are described by Ibar et al. (in preparation).

We obtained new 1.4-GHz data for the SXDF, again using the VLA, during 2003. Many of these data were affected by interfer-

Table 1. Radio properties of SMGs in the Lockman Hole SHADES Source Catalogue.

Nickname	Position at 850 μm $\alpha_{\rm J2000}$ h m s	$\delta_{\rm J2000}$ ° ′ ″	$S_{850\mu m}$ $(S+, S-)$ /mJy	SNR^a	Position at 1.4 GHz $\alpha_{\rm J2000}$ h m s	$\delta_{\rm J2000}$ ° ′ ″	$S^b_{1.4\rm GHz}$ /μJy	Submm–radio separation^c /arcsec	P^c	Notes
LOCK850.01	10 52 01.417	+57 24 43.04	8.8 (1.0, 1.0)	8.54	10 52 01.249	+57 24 45.76	78.9 ± 4.7	3.04	**0.011**	z=2.148
LOCK850.02	10 52 57.316	+57 21 05.79	13.4 (2.1, 2.1)	6.83	10 52 57.014	+57 21 08.31	40.7 ± 5.6	3.51	**0.026**	
					10 52 57.084	+57 21 02.82	52.4 ± 5.6	3.51	**0.020**	
LOCK850.03	10 52 38.247	+57 24 36.54	10.9 (1.8, 1.9)	6.39	10 52 38.401	+57 24 39.50	35.0 ± 5.2	3.21	**0.027**	
					10 52 38.299	+57 24 35.76	25.8 ± 4.9	0.89	**0.005**	z=3.036
LOCK850.04	10 52 04.171	+57 26 58.85	10.6 (1.7, 1.8)	6.42	10 52 03.691	+57 27 07.06	47.0 ± 5.7	(9.08)	(0.104)	z=1.48
					10 52 04.079	+57 26 58.52	32.0 ± 5.1	0.81	**0.004**	
					10 52 04.226	+57 26 55.46	73.0 ± 5.0	3.42	**0.014**	
LOCK850.05	10 53 02.615	+57 18 26.95	8.1 (2.0, 2.1)	4.90	—	—	5σ < 22	—	—	24μm id
LOCK850.06	10 52 04.131	+57 25 26.34	6.8 (1.3, 1.3)	5.83	10 52 04.013	+57 25 24.20	15.0 ± 4.8	2.34	**0.038**	
					10 52 03.549	+57 25 17.38	22.2 ± 4.6	(10.1)	(0.176)	
LOCK850.07	10 53 01.403	+57 25 54.24	8.5 (1.8, 1.9)	5.30	10 53 00.956	+57 25 52.06	42.6 ± 5.8	4.22	**0.032**	
LOCK850.08	10 51 53.862	+57 18 39.75	5.4 (1.1, 1.2)	5.24	—	—	5σ < 22	—	—	24μm id
LOCK850.09	10 52 16.088	+57 25 04.11	5.9 (1.6, 1.6)	4.67	10 52 15.636	+57 25 04.26	52.6 ± 4.7	3.65	**0.021**	
LOCK850.10	10 52 48.607	+57 32 58.58	9.1 (2.7, 2.9)	4.53	10 52 48.992	+57 32 56.26	25.5 ± 6.3	3.87	**0.048**	
LOCK850.11	10 51 29.531	+57 24 05.21	6.2 (1.7, 1.8)	4.53	10 51 29.824	+57 24 15.19	19.0 ± 5.4	(10.3)	(0.181)	Confused at 24μm
LOCK850.12	10 52 27.612	+57 25 13.08	6.1 (1.7, 1.7)	4.58	10 52 27.579	+57 25 12.46	44.3 ± 5.1	0.67	**0.002**	z=2.14?
					10 52 28.793	+57 25 16.01	19.2 ± 4.5	(9.98)	(0.180)	
LOCK850.13	10 51 32.333	+57 31 34.76	5.6 (2.3, 2.9)	3.89	—	—	5σ < 28	—	—	
LOCK850.14	10 52 30.110	+57 22 15.55	7.2 (1.8, 1.9)	4.84	10 52 28.995	+57 22 22.42	25.3 ± 4.2	(11.3)	(0.178)	
					10 52 30.717	+57 22 09.56	37.4 ± 4.2	7.74	0.068	z=2.611
LOCK850.15	10 53 19.200	+57 21 10.64	13.2 (4.3, 5.0)	4.51	10 53 19.025	+57 21 09.47	43.9 ± 7.8	1.84	**0.009**	
					10 53 19.271	+57 21 08.45	61.5 ± 7.6	2.26	**0.009**	
					10 53 19.067	+57 21 16.28	22.6 ± 7.1	5.74	0.071	
LOCK850.16	10 51 51.453	+57 26 37.00	5.8 (1.8, 1.9)	4.32	10 51 51.690	+57 26 36.09	106 ± 6	2.12	**0.004**	z=1.147
					10 51 50.113	+57 26 35.73	115 ± 6	(10.9)	(0.059)	
LOCK850.17	10 51 58.250	+57 18 00.81	4.7 (1.3, 1.3)	4.49	10 51 58.018	+57 18 00.27	92.3 ± 4.5	1.96	**0.004**	z=2.239
LOCK850.18	10 52 27.693	+57 22 17.75	6.0 (1.9, 2.1)	4.27	10 52 27.778	+57 22 18.18	29.4 ± 4.4	0.81	**0.004**	z=1.956
					10 52 28.995	+57 22 22.42	25.3 ± 4.1	(11.5)	(0.178)	
LOCK850.19	10 52 35.709	+57 31 19.05	5.1 (2.0, 2.4)	3.92	—	—	5σ < 27	—	—	24μm id
LOCK850.21	10 52 56.858	+57 30 38.05	4.1 (2.0, 2.5)	3.62	—	—	5σ < 30	—	—	24μm id
LOCK850.22	10 51 37.551	+57 33 23.32	7.5 (3.2, 4.2)	4.00	—	—	5σ < 30	—	—	24μm id
LOCK850.23	10 52 13.737	+57 31 54.11	4.3 (1.9, 2.4)	3.71	—	—	5σ < 25	—	—	
LOCK850.24	10 52 00.227	+57 20 38.05	2.7 (1.2, 1.2)	3.60	10 52 00.445	+57 20 40.16	28.5 ± 4.8	2.75	**0.026**	
LOCK850.26	10 52 40.950	+57 23 12.01	5.8 (2.4, 2.9)	3.93	10 52 40.726	+57 23 15.18	14.5 ± 5.5	3.65	0.064	
					10 52 40.698	+57 23 09.96	31.4 ± 5.2	2.89	**0.026**	
					10 52 41.453	+57 23 20.65	1,050 ± 50	(9.55)	(0.004)	
LOCK850.27	10 52 03.574	+57 18 13.46	5.0 (1.3, 1.3)	4.63	10 52 04.579	+57 18 06.11	20.0 ± 4.5	(11.0)	(0.181)	
LOCK850.28	10 52 57.001	+57 31 07.14	6.4 (1.7, 1.8)	4.67	10 52 57.667	+57 30 58.71	63.0 ± 8.2	(9.99)	(0.091)	Candidate id
LOCK850.29	10 51 30.923	+57 20 35.95	6.7 (2.0, 2.2)	4.39	10 51 31.305	+57 20 40.28	23.7 ± 4.9	5.32	0.066	Radio+24μm id
LOCK850.30	10 52 07.786	+57 19 06.59	4.7 (1.5, 1.6)	4.19	10 52 07.490	+57 19 04.01	245 ± 13	3.52	**0.004**	z=2.689
					10 52 08.054	+57 19 02.58	20.0 ± 4.2	4.56	0.064	
LOCK850.31	10 52 16.055	+57 16 21.11	6.0 (1.8, 2.0)	4.34	10 52 15.989	+57 16 19.34	43.0 ± 4.7	1.85	**0.010**	
LOCK850.33	10 51 55.975	+57 23 11.76	3.8 (1.0, 1.1)	4.45	10 51 55.470	+57 23 12.77	51.0 ± 4.3	4.21	**0.027**	z=2.686
LOCK850.34	10 52 13.502	+57 33 28.14	14.0 (3.1, 3.2)	5.37	10 52 13.584	+57 33 20.81	28.7 ± 8.7	7.36	0.075	Radio+24μm id
					10 52 14.202	+57 33 28.30	58.4 ± 8.5	5.63	**0.035**	
LOCK850.35	10 52 46.915	+57 20 56.25	6.1 (2.2, 2.4)	4.12	10 52 46.655	+57 20 52.54	17.4 ± 5.0	4.27	0.065	
LOCK850.36	10 52 09.335	+57 18 06.78	6.3 (1.7, 1.8)	4.55	—	—	5σ < 20	—	—	
LOCK850.37	10 51 24.130	+57 23 34.86	7.5 (2.9, 3.5)	4.10	10 51 24.595	+57 23 31.08	14.8 ± 5.4	5.33	0.078	24μm id
					10 51 24.342	+57 23 36.18	41.8 ± 8.7	2.16	**0.013**	
LOCK850.38	10 53 07.104	+57 24 31.39	4.3 (2.2, 2.7)	3.63	10 53 07.253	+57 24 30.82	24.4 ± 6.7	1.33	**0.011**	
					10 53 06.568	+57 24 32.65	13.8 ± 6.5	4.51	0.075	
					10 53 06.933	+57 24 27.27	20.9 ± 6.2	4.35	0.059	
LOCK850.39	10 52 24.851	+57 16 09.80	6.5 (2.2, 2.5)	4.20	10 52 25.643	+57 16 07.65	5σ < 20	—	—	
LOCK850.40	10 52 02.014	+57 19 15.80	3.0 (1.1, 1.2)	3.79	10 52 01.721	+57 19 17.00	16.2 ± 4.3	2.66	**0.042**	
					10 52 02.070	+57 19 23.13	18.0 ± 4.9	7.34	0.075	
LOCK850.41	10 51 59.861	+57 24 23.60	3.8 (0.9, 1.0)	4.54	10 52 00.248	+57 24 21.69	43.6 ± 4.7	3.66	**0.026**	z=0.689
					10 51 59.760	+57 24 24.94	22.1 ± 4.8	1.57	**0.015**	
LOCK850.43	10 52 57.169	+57 23 51.81	4.9 (2.1, 2.6)	3.80	10 52 56.561	+57 23 52.80	25.4 ± 5.4	5.01	0.060	24μm id
					10 52 56.655	+57 23 54.13	19.4 ± 5.5	4.76	0.067	Train wreck?
					10 52 56.576	+57 23 58.62	40.8 ± 5.9	(8.33)	(0.105)	24μm id
LOCK850.47	10 52 35.629	+57 25 14.04	3.5 (1.7, 2.1)	3.54	10 52 35.138	+57 25 16.04	5σ < 22	—	—	
LOCK850.48	10 52 56.239	+57 32 45.82	5.4 (2.1, 2.5)	3.94	10 52 55.181	+57 32 45.38	43.7 ± 10.0	(8.53)	(0.103)	24μm id
LOCK850.52	10 52 45.531	+57 31 21.94	3.9 (2.2, 2.7)	3.52	10 52 45.808	+57 31 19.86	38.7 ± 8.0	3.05	**0.023**	
LOCK850.53	10 52 40.488	+57 19 28.42	4.4 (2.3, 2.9)	3.62	—	—	5σ < 21	—	—	24μm id
LOCK850.60	10 51 43.583	+57 24 45.97	3.1 (1.7, 2.0)	3.40	10 51 43.488	+57 24 35.90	22.3 ± 4.9	(10.1)	(0.176)	
LOCK850.63	10 51 53.906	+57 25 05.07	3.6 (1.2, 1.3)	4.00	10 51 54.261	+57 25 02.55	22.6 ± 4.8	3.82	**0.049**	
LOCK850.64	10 52 51.808	+57 32 42.23	5.8 (2.5, 3.2)	3.87	10 52 52.231	+57 32 32.39	45.5 ± 7.4	(10.4)	(0.124)	
					10 52 53.121	+57 32 40.22	31.7 ± 7.4	(10.8)	(0.159)	
LOCK850.66	10 51 38.687	+57 20 17.24	4.2 (1.9, 2.2)	3.74	—	—	5σ < 21	—	—	
LOCK850.67	10 52 08.998	+57 23 55.13	2.5 (1.5, 1.5)	3.30	—	—	5σ < 21	—	—	
LOCK850.70	10 51 48.516	+57 30 46.69	3.8 (2.2, 2.5)	3.52	10 51 47.894	+57 30 44.37	21.9 ± 7.2	5.52	0.070	24μm id

a) Raw signal-to-noise ratio (SNR), before deboosting.
b) Integrated flux densities; for tentative detections, these are given in *italics*.
c) Possible counterparts with 8.0–12.5-arcsec offsets are listed in parentheses for completeness. Reliable identifications ($P \leqslant 0.05$) are listed in **bold**.

Table 1. Cont...

Nickname	Position at 850μm		$S_{850\mu m}$	SNR	Position at 1.4 GHz		$S_{1.4\,GHz}$	Submm–radio separation	P	Notes
	α_{J2000} h m s	δ_{J2000} ° ′ ″	$(S+, S-)$ /mJy		α_{J2000} h m s	δ_{J2000} ° ′ ″	/μJy	/arcsec		
LOCK850.71	10 52 18.618	+57 19 03.79	3.9 (1.8, 2.0)	3.69	10 52 19.086	+57 18 57.87	95.8 ± 4.6	7.03	**0.030**	
LOCK850.73	10 51 41.660	+57 22 17.63	3.5 (1.9, 2.3)	3.48	10 51 41.705	+57 22 20.10	26.7 ± 4.6	2.50	**0.025**	
					10 51 41.992	+57 22 17.52	27.3 ± 4.8	2.69	**0.027**	
LOCK850.75	10 53 15.927	+57 26 45.47	4.4 (2.2, 2.6)	3.68	10 53 15.439	+57 26 37.42	27.1 ± 7.8	(8.96)	(0.150)	Radio+24μm id
LOCK850.76	10 51 48.516	+57 28 38.69	4.7 (2.5, 3.1)	3.66	10 51 49.101	+57 28 40.28	48.0 ± 6.0	4.98	**0.036**	
LOCK850.77	10 51 57.004	+57 22 10.07	3.2 (1.2, 1.3)	3.84	10 51 57.153	+57 22 09.58	*15.5 ± 4.4*	1.30	**0.017**	
					10 51 57.665	+57 22 12.35	39.5 ± 7.8	5.81	**0.050**	
LOCK850.78	10 51 45.333	+57 17 38.68	4.5 (2.2, 2.7)	3.70	—		$5\sigma < 23$	—	—	
LOCK850.79	10 51 52.104	+57 21 27.38	3.1 (1.3, 1.5)	3.65	10 51 52.594	+57 21 24.43	22.4 ± 4.5	4.94	0.064	24μm id
					10 51 51.198	+57 21 27.29	26.3 ± 4.6	7.33	0.077	Plausible id
LOCK850.81	10 52 31.989	+57 18 00.40	5.3 (1.9, 2.3)	4.01	10 51 31.523	+57 17 51.67	55.2 ± 5.3	(9.51)	(0.096)	
LOCK850.83	10 53 07.939	+57 28 39.14	3.1 (2.0, 2.1)	3.37	—		$5\sigma < 28$	—	—	24μm id
LOCK850.87	10 51 53.302	+57 17 33.38	3.4 (1.5, 1.7)	3.64	10 51 53.365	+57 17 30.05	84.5 ± 5.3	3.37	**0.012**	
LOCK850.100	10 51 39.056	+57 15 09.81	11.2 (4.2, 5.3)	4.30	10 51 38.877	+57 15 03.90	*19.8 ± 6.3*	6.09	0.077	Radio+24μm id

waveband of choice for the identification of counterparts at other wavelengths and several related objectives.

A radio source peaking at $\geqslant 4\,\sigma$ with an integrated flux density in excess of $3\,\sigma$, in either the high- or low-resolution images, where σ is the noise measured locally, is considered a *robust* detection. In the LH and SXDF, the surface densities of all radio sources above this threshold are $1.9 \pm 0.1\,\text{arcmin}^{-2}$ (Ivison et al. 2005) and $1.6 \pm 0.1\,\text{arcmin}^{-2}$, respectively. Where a robust detection does not exist, we list those sources peaking at $\geqslant 3\,\sigma$ with an integrated flux density in excess of $2\,\sigma$, these being considered *tentative* detections. Positions and flux densities were measured using JMFIT with multi-component fits: usually a Gaussian and a surface baseline, with an extra Gaussian component for close multiple radio sources. To enable us to make appropriate corrections for bandwidth smearing – the radio flavour of chromatic aberration which causes the peak flux density to fall as a function of distance from the pointing centre – measurements were made in images of each pointing rather than in the final, large mosaic. In cases where sources appeared in more than one 400-arcmin^2 pointing, error-weighted means were obtained.

For each SMG we have searched for potential radio (1.4-GHz) counterparts inside a positional error circle of radius 8 arcsec (see §4), also listing those within 12.5 arcsec for completeness. This relatively large search area ensures that no real associations are missed. At the extreme depths reached by the radio imaging reported here, the cumulative surface density of radio sources in the 8-arcsec-radius error circles yields one robust source in every ten search areas, though not all will be regarded as significant associations as we shall see shortly.

We have also searched for potential 24-μm counterparts inside a positional error circle of radius 8 arcsec, listing those within 15 arcsec for completeness (a slightly larger radius than for the radio counterparts to account for the larger 24-μm beam).

To quantify the formal significance of each of the potential submm/radio and submm/mid-IR associations we have used the method of Downes et al. (1986; see also Dunlop et al. 1989). This corrects the raw Poisson probability, P, that a radio or 24-μm source of the observed flux density could lie at the observed distance from the SMG, for the number of ways that such an apparently significant association could have been uncovered by chance.

The positions, flux densities and P values of all LH and SXDF radio and 24-μm counterparts are presented in Tables 1 through 4, adopting those counterparts within 8 arcsec with $P \leqslant 0.05$ as robust. P values for counterparts with larger separations are listed in

parenthesis, using search radii of 12.5 or 15 arcsec at 1.4 GHz and 24 μm, respectively. We have also searched for cases where *coincident* radio and 24-μm counterparts within 8 arcsec have $P_{1.4\,GHz}$ and $P_{24\,\mu m} \leqslant 0.10$, finding three such cases. Figs A1 and A2 contain 25-arcsec × 25-arcsec postage stamp images centred on the LH and SXDF SMG positions, respectively. Alternative names used for these SMGs in the literature are listed in Table 5.

Our identifications – based on radio and/or 24-μm data – are summarised in Table 6. Clements et al. (in preparation) and Dye et al. (in preparation) will present independent identification analyses in SXDF and LH, respectively, using optical and near-IR colours which are believed to provide a useful complement to deep radio imaging (e.g. Webb et al. 2003b; Pope et al. 2005).

Of the 32 identifications made in only one waveband – equal numbers in each field – 21 are radio counterparts, mainly in SXDF. Of these 21 SMGs, only seven have detections at 24 μm that have not made the grade via the P statistic. Of the 11 mid-IR-only identifications, five have radio counterparts just above our adopted $P \leqslant 0.05$ threshold.

In total, we find robust counterparts for two thirds (79) of the 120 sources in the SHADES Source Catalogue, entirely consistent with previous studies (Ivison et al. 2002, 2005; Pope et al. 2006).

4   ON THE UNCERTAINTY IN SMG POSITIONS

SCUBA-2 will herald a vast increase in the number of catalogued SMGs, covering tens of square degrees. Radio coverage of such areas at the depth employed here will not be trivial to acquire, even in the era of e-VLA and LOFAR. It is interesting, therefore, to speculate about whether our knowledge of panchromatic SMG properties will progress in the absence of radio detections (and hence accurate positions and counterparts at other wavelengths) for the majority of SMGs. Can we determine the significance of submm detections required to enable spectroscopic follow-up with modern integral-field unit (IFU) spectrometers such as KMOS on the 8-m Very Large Telescope (Sharples et al. 2006)?

Submm positions for the SHADES Source Catalogue were deduced by fitting to the beam pattern in an optimally filtered map (i.e. after smoothing with the beam), then averaging over four independent reductions of the same raw data (Coppin et al. 2006). One reduction adopted the centre of the nearest 3-arcsec pixel as the position, while the others used 1-arcsec pixels, so a small rounding error adds to the uncertainty. Ignoring this minor effect, the positional uncertainty should be $\Delta\alpha = \Delta\delta = 0.6\,\theta\,(\text{SNR})^{-1}$ in

Table 2. Radio properties of SMGs in the SXDF SHADES Source Catalogue.

Nickname	Position at 850μm		$S_{850\mu m}$	SNR^a	Position at 1.4 GHz		$S^b_{1.4\,\mathrm{GHz}}$	Submm–radio separation	P	Notes
	α_{J2000} h m s	δ_{J2000} $\circ$ ′ ″	$(S+, S-)$ /mJy		α_{J2000} h m s	δ_{J2000} $\circ$ ′ ″	/μJy	/arcsec		
SXDF850.01	02 17 30.531	-04 59 36.96	10.4 (1.5, 1.4)	7.35	02 17 30.629	-04 59 36.70	54.3 ± 9.7	1.49	**0.005**	
SXDF850.02	02 18 03.509	-04 55 27.24	10.1 (1.6, 1.6)	6.62	02 18 03.556	-04 55 27.55	66.2 ± 10.9	0.77	**0.001**	
SXDF850.03	02 17 42.144	-04 56 28.22	8.8 (1.5, 1.6)	5.95	02 17 42.128	-04 56 27.67	77.2 ± 9.3	0.60	**0.001**	
SXDF850.04	02 17 38.621	-05 03 37.47	4.4 (1.7, 2.0)	3.88	02 17 38.680	-05 03 39.46	185 ± 12	2.18	**0.002**	
SXDF850.05	02 18 02.876	-05 00 32.75	8.4 (1.7, 1.9)	5.35	02 18 02.858	-05 00 30.91	574 ± 10	1.86	**0.001**	
SXDF850.06	02 17 29.769	-05 03 26.81	8.2 (2.2, 2.2)	4.72	02 17 30.224	-05 03 25.37	66.6 ± 12.7	6.95	**0.034**	
					02 17 29.926	-05 03 22.01	47.4 ± 10.8	5.34	**0.033**	
					02 17 29.753	-05 03 18.50	92.9 ± 9.6	(8.31)	(0.044)	
SXDF850.07	02 17 38.921	-05 05 23.72	7.1 (1.5, 1.6)	5.16	02 17 38.878	-05 05 28.03	41.2 ± 11.3	4.36	**0.029**	
SXDF850.08	02 17 44.432	-04 55 54.72	6.0 (1.8, 1.9)	4.39	02 17 44.137	-04 55 48.72	52.0 ± 9.5	7.45	**0.042**	
SXDF850.09	02 17 56.422	-04 58 06.74	6.4 (2.0, 2.1)	4.35	02 17 55.772	-04 58 14.31	46.0 ± 10.5	(12.3)	(0.110)	
SXDF850.10	02 18 25.248	-04 55 57.21	7.7 (2.6, 3.1)	4.24	02 18 24.975	-04 56 02.85	149 ± 12	6.97	**0.017**	
					02 18 25.797	-04 55 51.31	47.4 ± 10.4	(10.1)	(0.094)	
SXDF850.11	02 17 25.117	-04 59 37.44	4.5 (1.9, 2.2)	3.81	02 17 25.101	-04 59 33.77	56.8 ± 10.0	3.68	**0.018**	
SXDF850.12	02 17 59.369	-05 05 03.74	5.7 (1.7, 1.8)	4.34	02 17 59.294	-05 05 04.04	42.0 ± 10.8	1.16	**0.004**	
SXDF850.14	02 18 19.256	-05 02 44.21	4.8 (1.9, 2.1)	3.93	02 18 18.748	-05 02 49.25	30.4 ± 11.4	(9.11)	(0.109)	
					02 18 19.018	-05 02 48.90	40.0 ± 11.1	5.89	**0.040**	
SXDF850.15	02 18 15.699	-04 54 05.22	6.2 (1.6, 1.6)	4.76	—	—	$5\sigma < 37$	—	—	
SXDF850.16	02 18 13.887	-04 57 41.74	4.8 (1.7, 1.8)	4.10	02 18 13.805	-04 57 43.22	36.5 ± 8.8	1.92	**0.011**	
SXDF850.17	02 17 54.980	-04 53 02.83	7.6 (1.7, 1.7)	5.25	—	—	$5\sigma < 39$	—	—	
SXDF850.18	02 17 57.790	-05 00 29.75	6.4 (2.0, 2.2)	4.30	02 17 57.591	-05 00 33.69	40.8 ± 9.0	4.94	**0.034**	
SXDF850.19	02 18 28.149	-04 58 39.21	4.3 (1.8, 2.1)	3.79	02 18 27.782	-04 58 37.17	95.9 ± 10.1	5.86	**0.020**	
SXDF850.20	02 17 44.182	-05 02 15.97	4.4 (2.0, 2.2)	3.78	—	—	$5\sigma < 34$	—	—	
SXDF850.21	02 17 42.803	-05 04 27.71	5.2 (2.0, 2.2)	3.99	02 17 42.499	-05 04 24.50	690 ± 50	5.56	**0.002**	
SXDF850.22	02 18 00.379	-05 07 41.50	6.2 (2.3, 2.6)	4.08	—	—	$5\sigma < 36$	—	—	
SXDF850.23	02 17 42.526	-05 05 45.47	5.2 (1.7, 2.0)	4.12	02 17 42.455	-05 05 45.88	71.3 ± 10.1	1.14	**0.002**	
SXDF850.24	02 17 34.578	-05 04 37.71	5.1 (2.0, 2.3)	3.93	02 17 34.696	-05 04 39.18	35.3 ± 10.3	2.30	**0.014**	
					02 17 34.749	-05 04 30.47	42.3 ± 12.0	7.68	**0.047**	
SXDF850.25	02 18 12.120	-05 05 55.74	4.0 (2.1, 2.5)	3.58	—	—	$5\sigma < 38$	—	—	
SXDF850.27	02 18 07.861	-05 01 48.49	5.6 (2.0, 2.3)	4.08	02 18 07.934	-05 01 45.38	316 ± 12	3.30	**0.002**	
SXDF850.28	02 18 07.043	-04 59 15.50	4.8 (2.2, 2.7)	3.76	02 18 06.920	-04 59 12.72	96.7 ± 10.4	3.34	**0.009**	
					02 18 06.831	-04 59 17.52	96.2 ± 9.6	3.76	**0.011**	
					02 18 06.419	-04 59 20.05	57.9 ± 9.0	(10.4)	(0.085)	
SXDF850.29	02 18 16.468	-04 55 11.82	5.3 (1.8, 1.9)	4.15	02 18 16.484	-04 55 08.66	245 ± 9	3.17	**0.003**	
SXDF850.30	02 17 40.305	-05 01 16.22	5.7 (2.0, 2.2)	4.14	02 17 40.020	-05 01 15.32	29.3 ± 11.3	4.35	**0.037**	
SXDF850.31	02 17 36.301	-04 55 57.46	6.0 (1.7, 2.0)	4.37	02 17 35.856	-04 55 55.10	55.9 ± 11.8	7.07	**0.039**	
SXDF850.32	02 17 22.888	-05 00 38.10	6.0 (2.4, 3.0)	3.96	—	—	$5\sigma < 40$	—	– -	
SXDF850.35	02 18 00.888	-04 53 11.24	5.3 (1.8, 2.1)	4.06	02 18 00.867	-04 53 05.71	45.1 ± 11.3	5.54	**0.035**	
SXDF850.36	02 18 32.272	-04 59 47.21	5.4 (1.8, 1.9)	4.20	—	—	$5\sigma < 38$	—	—	
SXDF850.37	02 17 24.445	-04 58 39.93	4.5 (2.2, 2.6)	3.71	02 17 24.569	-04 58 41.29	40.9 ± 9.2	2.30	**0.013**	
SXDF850.38	02 18 25.427	-04 57 14.71	3.8 (2.3, 2.7)	3.49	02 18 25.176	-04 57 19.70	49.8 ± 18.2	6.25	**0.037**	
SXDF850.39	02 17 50.595	-04 55 40.16	4.0 (1.7, 2.1)	3.69	—	—	$5\sigma < 37$	—	—	
SXDF850.40	02 17 29.669	-05 00 59.21	3.6 (1.5, 1.6)	3.78	02 17 29.625	-05 00 58.57	40.3 ± 9.5	0.92	**0.003**	
SXDF850.45	02 18 29.328	-05 05 40.71	21.9 (6.2, 6.8)	4.92	—	—	$5\sigma < 40$	—	—	
SXDF850.47	02 17 33.887	-04 58 57.71	3.0 (1.6, 1.9)	3.39	02 17 34.363	-04 58 57.23	175 ± 11	7.15	**0.015**	
					02 17 34.400	-04 58 59.76	43.1 ± 10.1	7.95	**0.048**	
					02 17 33.616	-04 58 58.21	64.2 ± 13.2	4.09	**0.018**	
SXDF850.48	02 17 24.621	-04 57 17.68	7.6 (2.5, 2.9)	4.28	—	—	$5\sigma < 39$	—	—	
SXDF850.49	02 18 20.259	-04 56 48.47	3.3 (2.0, 2.2)	3.43	—	—	$5\sigma < 35$	—	—	
SXDF850.50	02 18 02.858	-04 56 45.49	5.3 (2.0, 2.5)	3.93	02 18 02.827	-04 56 47.80	38.8 ± 12.7	2.36	**0.014**	
SXDF850.52	02 18 04.896	-05 04 53.74	3.2 (1.8, 2.1)	3.41	02 18 05.118	-05 04 52.12	89.3 ± 11.1	3.69	**0.011**	
					02 18 04.972	-05 05 01.02	88.8 ± 10.3	7.37	**0.029**	
SXDF850.55	02 17 52.190	-05 04 46.50	3.9 (2.2, 2.7)	3.52	02 17 51.865	-05 04 46.96	41.7 ± 13.8	4.88	**0.033**	
SXDF850.56	02 17 50.679	-05 06 31.82	3.6 (2.2, 2.5)	3.47	—	—	$5\sigma < 40$	—	—	
SXDF850.63	02 17 45.802	-04 57 50.49	4.1 (1.7, 2.1)	3.73	—	—	$5\sigma < 38$	—	—	
SXDF850.65	02 18 07.935	-05 04 03.24	4.3 (1.9, 2.4)	3.70	—	—	$5\sigma < 27$	—	—	
SXDF850.69	02 17 51.395	-05 02 50.82	3.6 (2.1, 2.4)	3.49	—	—	$5\sigma < 38$	—	—	$61.4 \pm 10.4\,\mu$Jy, 13.0$''$ to SSW
SXDF850.70	02 18 11.199	-05 02 47.16	4.0 (1.9, 2.3)	3.64	—	—	$5\sigma < 29$	—	—	
SXDF850.71	02 18 21.235	-04 59 03.22	4.1 (1.9, 2.4)	3.66	—	—	$5\sigma < 35$	—	—	24μm id
SXDF850.74	02 17 58.732	-04 54 28.83	3.3 (1.8, 2.1)	3.45	02 17 58.729	-04 54 33.41	38.9 ± 12.7	4.58	**0.032**	
SXDF850.76	02 17 55.781	-05 06 21.82	4.4 (2.0, 2.4)	3.73	02 17 56.308	-05 06 24.91	84.2 ± 13.1	(8.46)	(0.049)	
SXDF850.77	02 17 36.432	-05 04 32.15	3.0 (2.0, 2.1)	3.35	02 17 35.951	-05 04 25.97	43.8 ± 10.7	(9.48)	(0.093)	
					02 17 36.175	-05 04 33.26	34.0 ± 9.9	4.00	**0.047**	
SXDF850.86	02 18 17.184	-05 04 04.70	3.6 (1.9, 2.2)	3.54	—	—	$5\sigma < 37$	—	—	
SXDF850.88	02 18 00.994	-05 04 48.49	4.5 (2.1, 2.5)	3.74	02 18 01.494	-05 04 43.74	40.8 ± 9.3	(8.85)	(0.091)	$54.5 \pm 10.8\,\mu$Jy, 12.6$''$ to ESE
SXDF850.91	02 17 34.808	-04 57 23.93	3.5 (2.1, 2.5)	3.43	—	—	$5\sigma < 35$	—	—	
SXDF850.93	02 17 33.082	-04 58 13.48	3.1 (2.0, 2.1)	3.36	—	—	$5\sigma < 28$	—	—	
SXDF850.94	02 17 40.079	-04 58 17.73	4.1 (1.8, 2.1)	3.75	—	—	$5\sigma < 41$	—	—	
SXDF850.95	02 17 41.715	-04 58 33.70	3.4 (1.9, 2.2)	3.47	—	—	$5\sigma < 35$	—	—	
SXDF850.96	02 18 00.000	-05 02 12.75	4.7 (2.1, 2.5)	3.79	02 18 00.238	-05 02 16.83	37.5 ± 8.4	5.41	**0.039**	$85.3 \pm 9.9\,\mu$Jy, 12.7$''$ to NNW
SXDF850.119	02 17 56.345	-04 52 55.24	4.5 (2.1, 2.5)	3.73	02 17 56.205	-04 53 03.36	71.9 ± 8.7	(8.39)	(0.056)	
					02 17 56.005	-04 52 51.96	38.0 ± 9.7	6.06	**0.043**	

a) Raw SNR, before deboosting.

b) Flux densities for tentative detections are given in *italics*.

c) Possible counterparts with 8.0–12.5-arcsec offsets are listed in parentheses for completeness. Reliable identifications ($P \leqslant 0.05$) are listed in **bold**.

Table 3. Mid-IR properties of SMGs in the LH SHADES Source Catalogue.

Nickname	Position at 24 μm		ID[a]	$S_{24\mu m}$ /μJy	Off -set ''	P[b]
	α_{J2000} h m s	δ_{J2000} ° ' ''				
LOCK850.01	10 52 01.30	+57 24 46.1	1934	217 ± 16	3.20	**0.024**
LOCK850.02	10 52 57.07	+57 21 02.9	19460	545 ± 31	3.51	**0.010**
LOCK850.03	10 52 38.66	+57 24 43.7	17451	73.7 ± 21.3	7.90	0.196
	10 52 38.31	+57 24 39.5	20054	183 ± 33	3.00	**0.026**
	10 52 38.31	+57 24 34.8	20603	175 ± 23	1.81	**0.012**
LOCK850.04	10 52 04.21	+57 26 55.6	15970	261 ± 73	3.27	**0.020**
	10 52 04.04	+57 26 58.3	15971	179 ± 68	1.19	**0.006**
	10 52 03.67	+57 27 07.0	3707	$1,104 \pm 33$	(9.10)	(0.026)
LOCK850.05	10 53 02.86	+57 18 23.9	11921	58.6 ± 15.1	3.64	0.107
LOCK850.06	10 52 04.12	+57 25 25.8	11922	75.1 ± 12.7	0.55	**0.005**
	10 52 03.51	+57 25 17.1	17409	379 ± 18	(10.5)	(0.107)
	10 52 05.19	+57 25 22.9	20753	540 ± 48	(9.22)	(0.060)
LOCK850.07	10 53 00.97	+57 25 52.2	5670	341 ± 21	4.05	**0.021**
LOCK850.08	10 51 53.69	+57 18 34.9	1811	481 ± 25	5.05	**0.021**
LOCK850.09	10 52 15.73	+57 25 01.7	13577	159 ± 73	3.76	**0.043**
	10 52 15.65	+57 25 04.5	13578	466 ± 74	3.56	**0.012**
LOCK850.10	10 52 47.39	+57 32 57.9	16088	65.9 ± 11.1	(9.82)	(0.429)
	10 52 48.27	+57 32 51.0	17604	79.6 ± 10.8	(8.05)	(0.313)
LOCK850.11	10 51 29.16	+57 24 06.8	8740	112 ± 57	3.39	0.053
	10 51 29.39	+57 24 10.3	8741	177 ± 51	5.22	0.063
	10 51 29.81	+57 24 16.3	8742	111 ± 17	(11.3)	(0.349)
LOCK850.12	10 52 27.60	+57 25 12.4	3757	263 ± 19	0.69	**0.001**
LOCK850.13	10 51 31.45	+57 31 29.1	11931	240 ± 17	(9.09)	(0.137)
	10 51 31.77	+57 31 41.2	11932	172 ± 14	7.88	0.110
LOCK850.14	10 52 30.72	+57 22 09.4	5560	188 ± 16	7.88	0.102
	10 52 29.06	+57 22 21.8	5563	103 ± 13	(10.5)	(0.343)
LOCK850.15	10 53 19.26	+57 21 08.3	3834	353 ± 20	2.39	**0.009**
	10 53 18.99	+57 21 15.6	3836	70.4 ± 12.1	5.24	0.141
LOCK850.16	10 51 51.67	+57 26 36.0	3626	314 ± 24	2.02	**0.008**
LOCK850.17	10 51 58.48	+57 18 01.2	13387	64.2 ± 26.1	1.90	**0.040**
	10 51 57.96	+57 17 59.9	17315	239 ± 18	2.52	**0.015**
LOCK850.18	10 52 29.06	+57 22 21.8	5563	103 ± 13	(11.8)	(0.381)
LOCK850.19	10 52 36.09	+57 31 19.6	13661	118 ± 15	3.12	**0.045**
	10 52 35.52	+57 31 11.7	17536	242 ± 19	7.51	0.076
	10 52 35.06	+57 31 23.7	17539	221 ± 36	7.00	0.075
LOCK850.21	10 52 56.79	+57 30 37.9	2832	97.9 ± 14.1	0.57	**0.004**
	10 52 57.80	+57 30 35.3	2833	124 ± 18	(8.07)	(0.218)
LOCK850.22	10 51 37.09	+57 33 16.9	2895	402 ± 21	7.41	0.113
	10 51 36.68	+57 33 32.8	2896	377 ± 20	(11.8)	(0.127)
LOCK850.23	10 52 12.83	+57 32 00.5	2722	116 ± 17	(9.70)	(0.288)
	10 52 14.71	+57 31 54.7	17516	57.3 ± 11.3	7.86	0.213
LOCK850.24	10 52 00.45	+57 20 39.7	1842	455 ± 21	2.45	**0.007**
LOCK850.26	10 52 41.13	+57 23 19.8	239	75.9 ± 12.7	7.92	0.193
	10 52 40.66	+57 23 09.7	5601	195 ± 16	3.29	**0.029**
LOCK850.27	10 52 03.45	+57 18 19.3	1984	106 ± 15	5.93	0.117
	10 52 04.77	+57 18 05.9	1986	196 ± 13	(12.3)	(0.247)
LOCK850.28	10 52 57.69	+57 30 58.6	13901	252 ± 14	(10.2)	(0.154)
LOCK850.29	10 51 31.65	+57 20 40.8	18689	111 ± 14	7.63	0.149
LOCK850.30	10 52 07.68	+57 19 04.1	2004	233 ± 19	2.63	**0.016**
LOCK850.31	10 52 15.96	+57 16 19.2	3434	467 ± 19	2.06	**0.005**
LOCK850.33	10 51 55.40	+57 23 12.9	1917	104 ± 14	4.79	0.091
LOCK850.34	10 52 13.66	+57 33 21.3	2932	93.5 ± 12.0	6.96	0.153
	10 52 14.21	+57 33 27.9	2933	84.9 ± 16.7	5.70	0.134
	10 52 13.97	+57 33 32.8	2934	128 ± 19	5.99	0.101
LOCK850.35	10 52 46.46	+57 20 56.8	153	51.0 ± 12.7	3.72	0.124
	10 52 45.94	+57 20 51.4	15952	161 ± 14	(9.26)	(0.206)
	10 52 46.42	+57 21 06.6	15953	110 ± 38	(11.1)	(0.346)
	10 52 46.91	+57 21 06.1	15954	108 ± 34	(9.85)	(0.309)
	10 52 47.94	+57 21 01.3	19555	75.0 ± 11.4	(9.71)	(0.393)
LOCK850.36	—	—	—	$5\sigma < 60$	—	—
LOCK850.37	10 51 24.60	+57 23 31.0	1870	250 ± 17	5.42	**0.047**
	10 51 24.27	+57 23 41.4	17334	126 ± 16	6.64	0.116
LOCK850.38	10 53 07.06	+57 24 31.6	5682	260 ± 16	0.41	**0.001**
LOCK850.39	—	—	—	$5\sigma < 60$	—	—
LOCK850.40	10 52 01.54	+57 19 15.9	1994	91.9 ± 15.0	3.84	0.077
	10 52 03.07	+57 19 23.5	1997	85.2 ± 14.0	(11.5)	(0.422)
LOCK850.41	10 52 00.24	+57 24 21.5	13508	475 ± 37	3.71	**0.013**
	10 51 59.81	+57 24 25.1	13509	651 ± 46	1.56	**0.002**
	10 51 59.27	+57 24 13.3	17394	108 ± 15	(11.4)	(0.358)
	10 52 00.19	+57 24 15.3	17395	212 ± 22	(8.72)	(0.147)
LOCK850.43	10 52 56.64	+57 23 51.4	5780	261 ± 24	4.30	**0.031**
	10 52 56.61	+57 23 58.0	5781	456 ± 35	7.66	**0.042**
LOCK850.47	10 52 34.85	+57 25 04.6	17453	107 ± 16	(11.3)	(0.359)

Table 3. Cont...

Nickname	Position at 24 μm		ID	$S_{24\mu m}$ /μJy	Off -set ''	P
	α_{J2000} h m s	δ_{J2000} ° ' ''				
LOCK850.48	10 52 56.03	+57 32 42.3	18826	203 ± 17	3.90	**0.035**
	10 52 55.37	+57 32 46.5	20105	85.2 ± 13.7	7.03	0.165
LOCK850.52	10 52 46.16	+57 31 20.2	18804	561 ± 86	5.36	**0.019**
	10 52 45.76	+57 31 20.6	20079	310 ± 35	2.28	**0.009**
LOCK850.53	10 52 40.29	+57 19 24.4	13519	168 ± 15	4.33	**0.050**
LOCK850.60	10 51 43.50	+57 24 35.8	1941	150 ± 15	(10.2)	(0.247)
	10 51 43.90	+57 24 43.6	13512	87.8 ± 12.0	3.49	0.070
	10 51 43.08	+57 24 52.2	13513	82.5 ± 13.4	7.44	0.176
	10 51 43.81	+57 24 54.9	13514	109 ± 15	(9.12)	(0.282)
LOCK850.63	10 51 53.43	+57 25 06.2	1925	53.0 ± 13.0	4.01	0.130
	10 51 54.27	+57 25 02.7	1931	236 ± 17	3.78	**0.029**
	10 51 55.24	+57 24 59.3	1932	79.1 ± 12.0	(12.2)	(0.461)
LOCK850.64	10 52 51.67	+57 32 48.7	2740	88.5 ± 12.5	6.56	0.150
	10 52 52.57	+57 32 48.9	2741	53.1 ± 11.8	(9.06)	(0.454)
	10 52 52.32	+57 32 33.0	12103	425 ± 25	(10.1)	(0.089)
LOCK850.66	10 51 39.57	+57 20 27.1	13365	71.2 ± 12.1	(12.2)	(0.484)
LOCK850.67	10 52 08.07	+57 23 48.0	2044	102 ± 14	(10.4)	(0.340)
	10 52 08.87	+57 23 56.3	2045	108 ± 14	1.56	**0.017**
LOCK850.70	10 51 47.88	+57 30 44.6	2571	106 ± 12	5.53	0.108
LOCK850.71	10 52 19.10	+57 18 57.3	3487	181 ± 20	7.57	0.100
	10 52 19.53	+57 19 04.8	3488	54.3 ± 16.0	7.46	0.212
LOCK850.73	10 51 41.92	+57 22 18.6	1855	278 ± 19	2.32	**0.011**
LOCK850.75	10 53 15.19	+57 26 45.9	5713	147 ± 17	5.96	0.089
	10 53 15.02	+57 26 53.2	5714	150 ± 16	(10.7)	(0.260)
	10 53 15.52	+57 26 37.1	16059	262 ± 18	(8.99)	(0.124)
LOCK850.76	10 51 49.12	+57 28 40.1	2512	592 ± 26	5.07	**0.016**
LOCK850.77	10 51 56.99	+57 22 08.4	3602	51.7 ± 13.1	1.67	**0.042**
	10 51 57.57	+57 22 13.4	3603	154 ± 15	5.66	0.080
	10 51 56.23	+57 22 12.3	3608	55.4 ± 13.5	6.65	0.199
LOCK850.78	10 51 43.93	+57 17 44.9	1734	85.6 ± 14.7	(13.0)	(0.462)
LOCK850.79	10 51 51.22	+57 21 27.8	1884	92.8 ± 13.1	7.16	0.158
	10 51 52.63	+57 21 24.4	1892	292 ± 18	5.20	**0.037**
LOCK850.81	10 52 31.52	+57 17 51.6	17353	$3,667 \pm 51$	(9.59)	(0.007)
LOCK850.83	10 53 07.17	+57 28 40.0	2815	344 ± 25	6.26	**0.041**
LOCK850.87	10 51 53.36	+57 17 30.5	1975	399 ± 22	2.92	**0.011**
LOCK850.100	10 51 38.76	+57 15 04.7	1623	118 ± 13	5.65	0.101

a) Used to identify sources in Fig. A1.

b) P was calculated using a search radius of 8 arcsec. For possible counterparts with 8–15-arcsec offsets, P was calculated using a search radius of 15 arcsec — these values are listed in parentheses. Reliable identifications ($P \leqslant 0.05$) within 8 arcsec are listed in **bold**.

the limit where centroiding uncertainty dominates over systematic astrometry errors and for uncorrelated Gaussian noise. Here, $\Delta\alpha$ and $\Delta\delta$ are the r.m.s. errors in R.A. and Dec., respectively, θ is the FWHM of the submm beam and SNR is the signal-to-noise ratio after correction for flux boosting (see Appendix B for derivations).

We can use our radio associations, which should provide near-perfect positions, to check whether the uncertainties in submm position are consistent with this theoretical expectation, given the size of the JCMT's beam and the SNR of the 850-μm sources.

For a Gaussian distribution of errors in R.A. and Dec., the distribution of radial offsets ($re^{-r^2/2\sigma^2}$) peaks at σ ($= \Delta\alpha = \Delta\delta$). This peak bounds only 39.3 per cent of sources, with 68 per cent of the anticipated radial offsets lying within 1.51σ (close to, but not precisely equal to $\sqrt{2} \times \sigma$). 86.5, 95.6 and 98.9 per cent of offsets are expected to lie within 2σ, 2.5σ and 3σ, respectively.

Fig. 2 shows a histogram of offsets between the positions of the SMGs and those of all the radio counterparts listed in Tables 1 and 2. Here, α and δ represent the R.A./$\cos\delta$ and Dec. offsets between submm and radio positions; radial offsets are thus $\sqrt{\alpha^2 + \delta^2}$. The value of σ observed in Fig. 2 is approximately 3 arcsec so our adopted search radius of 8 arcsec (§3) corresponds to $\sim 2.5\sigma$ and should thus include ~ 95 per cent of all genuine radio identifications; moreover, since the typical deboosted SNR of the submm sources is ~ 3 (Coppin et al. 2006), the theoretical expectation is also $\sigma \sim 3$ arcsec (from equation 2 of Appendix B for $\theta = 14.5$ arcsec and SNR $= 3$). It is clear, therefore, that the observed distribution of radial offsets for the radio identifications is at least comparable with theoretical expectations.

Table 4. Mid-IR properties of SMGs in the SXDF SHADES Source Catalogue.

Nickname	Position at 24 μm		$S^a_{24\mu m}$	Off	P^b
	α_{J2000} h m s	δ_{J2000} $\circ$ ′ ″	/μJy	-set ″	
SXDF850.01	02 17 29.59	−04 59 36.6	485 ± 47	(14.1)	(0.109)
SXDF850.02	02 18 03.54	−04 55 26.9	313 ± 47	0.58	**0.001**
SXDF850.04	02 17 38.69	−05 03 39.2	488 ± 47	2.01	**0.005**
SXDF850.05	02 18 02.83	−05 00 31.0	956 ± 47	1.88	**0.002**
SXDF850.06	02 17 29.77	−05 03 19.6	873 ± 47	7.21	**0.017**
	02 17 29.91	−05 03 33.3	179 ± 47	6.82	0.060
	02 17 30.15	−05 03 24.2	532 ± 47	6.26	**0.023**
SXDF850.07	02 17 38.86	−05 05 29.1	325 ± 47	5.46	**0.031**
SXDF850.08	02 17 43.98	−04 55 52.1	221 ± 47	7.26	0.056
SXDF850.10	02 18 25.61	−04 55 59.2	153 ± 47	5.78	0.057
	02 18 24.88	−04 56 03.3	177 ± 47	(8.21)	(0.132)
SXDF850.11	02 17 25.16	−04 59 35.0	195 ± 47	2.52	**0.017**
SXDF850.12	02 17 58.60	−05 05 03.8	397 ± 47	(11.5)	(0.101)
SXDF850.14	02 18 19.58	−05 02 32.2	256 ± 47	(13.0)	(0.161)
	02 18 18.77	−05 02 49.0	240 ± 47	(8.70)	(0.110)
SXDF850.16	02 18 14.41	−04 57 49.0	247 ± 47	(10.7)	(0.136)
SXDF850.17	02 17 55.11	−04 52 50.5	174 ± 47	(12.5)	(0.195)
SXDF850.19	02 18 27.83	−04 58 36.7	536 ± 47	5.40	**0.019**
SXDF850.21	02 17 42.54	−05 04 25.8	6,844 ± 47	4.37	**0.001**
SXDF850.24	02 17 34.87	−05 04 32.7	381 ± 47	6.64	**0.034**
SXDF850.27	02 18 07.93	−05 01 44.8	334 ± 47	3.83	**0.018**
SXDF850.28	02 18 06.32	−04 59 14.3	176 ± 47	(10.9)	(0.175)
	02 18 06.43	−04 59 20.3	477 ± 47	(10.4)	(0.075)
	02 18 06.87	−04 59 12.4	877 ± 47	4.04	**0.007**
SXDF850.29	02 18 16.49	−04 55 08.2	971 ± 47	3.63	**0.005**
SXDF850.30	02 17 40.00	−05 01 15.1	523 ± 47	4.69	**0.016**
SXDF850.31	02 17 36.75	−04 56 10.4	452 ± 47	(14.6)	(0.120)
	02 17 35.83	−04 55 56.7	594 ± 47	7.10	**0.025**
	02 17 36.37	−04 56 03.4	251 ± 47	6.03	**0.043**
SXDF850.32	02 17 22.58	−05 00 44.4	168 ± 47	7.80	0.066
SXDF850.35	02 18 00.86	−04 53 06.6	215 ± 47	4.66	**0.036**
SXDF850.36	02 18 31.92	−04 59 59.1	162 ± 47	(13.0)	(0.205)
	02 18 31.95	−04 59 53.2	177 ± 47	7.69	0.065
	02 18 33.04	−04 59 41.4	181 ± 47	(12.9)	(0.195)
	02 18 31.86	−04 59 37.3	182 ± 47	(11.7)	(0.181)
SXDF850.37	02 17 24.41	−04 58 42.0	183 ± 47	2.14	**0.015**
SXDF850.45	02 18 30.11	−05 05 35.4	157 ± 47	(12.8)	(0.206)
SXDF850.47	02 17 34.37	−04 58 59.9	298 ± 47	7.56	**0.048**
	02 17 33.72	−04 58 58.7	250 ± 47	2.69	**0.015**
SXDF850.52	02 18 05.09	−05 04 52.7	151 ± 47	3.08	**0.029**
SXDF850.56	02 17 51.23	−05 06 30.5	299 ± 47	(8.34)	(0.086)
SXDF850.69	02 17 51.77	−05 02 58.6	157 ± 47	(9.59)	(0.168)
	02 17 51.06	−05 03 02.8	724 ± 47	(13.0)	(0.068)
SXDF850.71	02 18 21.28	−04 58 58.8	404 ± 47	4.47	**0.019**
SXDF850.76	02 17 56.32	−05 06 25.5	183 ± 47	(8.86)	(0.140)
SXDF850.77	02 17 36.02	−05 04 28.2	726 ± 47	7.32	**0.021**
	02 17 36.51	−05 04 25.6	295 ± 47	6.65	**0.042**
SXDF850.86	02 18 16.66	−05 04 00.0	208 ± 47	(9.13)	(0.131)
SXDF850.88	02 18 01.54	−05 04 42.1	446 ± 47	(10.4)	(0.079)
SXDF850.91	02 17 34.24	−04 57 14.3	203 ± 47	(12.9)	(0.184)
SXDF850.94	02 17 40.26	−04 58 24.0	187 ± 47	6.83	0.059
	02 17 39.24	−04 58 13.1	198 ± 47	(13.4)	(0.192)
SXDF850.96	02 18 00.40	−05 02 01.5	478 ± 47	(12.7)	(0.097)
SXDF850.119	02 17 56.20	−04 53 02.1	784 ± 47	7.20	**0.019**
	02 17 55.65	−04 52 58.0	202 ± 47	(10.8)	(0.158)
	02 17 56.24	−04 52 50.9	275 ± 47	4.62	**0.029**

a) Objects missing here, but listed in Table 2, have upper limits of $5\sigma < 235\,\mu$Jy at 24 μm.
b) P was calculated using a search radius of 8 arcsec. For possible counterparts with 8–15-arcsec offsets, P was calculated using a search radius of 15 arcsec — these values are listed in parentheses. Reliable identifications ($P \leqslant 0.05$) within 8 arcsec are listed in **bold**.

We can quantify this more precisely in two ways. First, we can use the distribution of radial offsets for all radio identification counterparts and attempt to correct statistically for background contamination: the dashed line in Fig. 2 represents the distribution and absolute level of a randomly distributed radio population with the counts seen in the LH radio image (§2.1). The number of radio identifications within a 6-arcsec radius of the submm positions is seen to exceed the random level by almost two orders of magnitude, which gives us (additional) confidence that the vast majority of the radio identifications are truly associated with the SMGs. The finite

Table 5. Alternative names for the SHADES Source Catalogue.

SHADES LOCK J—	LOCK–	8-mJy[a] LE850.–	MAMBO[b] LE1200.–	Bolocam[c] LE1100.–	Chapman[d] SMM J–
105201+572443	850.01	01	005	14	105201.25+572445.7
105257+572105	850.02	–	004	01	–
105238+572436	850.03	02	001	08	105238.30+572435.8
105204+572658	850.04	14	003	–	–
105204+572526	850.06	04	–	–	–
105153+571839	850.08	27	104	–	–
105216+572504	850.09	29	042	–	–
105227+572513	850.12	16	006	16	105227.58+572512.4
105230+572215	850.14	06	010	05	105230.73+572209.5
105151+572637	850.16	07	096	–	105151.69+572636.0
105158+571800	850.17	03	011	–	105158.02+571800.2
105227+572217	850.18	–	009	–	105227.77+572218.2
105200+572038	850.24	32	–	–	–
105203+571813	850.27	–	007	04	–
105130+572036	850.29	11	–	–	–
105207+571906	850.30	12	–	–	105207.49+571904.0
105155+572311	850.33	18	012	–	105155.47+572312.7
105202+571915	850.40	21	–	–	–
105159+572423	850.41	08	014	17	105200.22+572420.2
105148+572838	850.76	–	–	15	–

a) Scott et al. (2002).
b) Greve et al. (2004); Ivison et al. (2005).
c) Laurent et al. (2005).
d) Chapman et al. (2005).
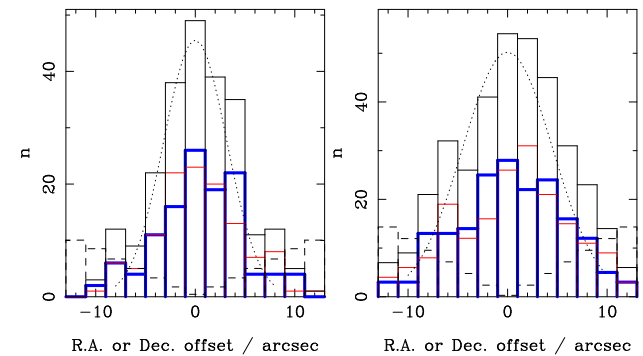
Figure 2. Histograms of positional offsets between the positions of the SMGs and those of the counterparts (*left:* radio; *right:* 24 μm), in R.A. (α, thick blue), Dec. (δ, red) and both together (black). The dashed lines show the expected distribution and absolute level for a randomly distributed population with the average counts seen in the LH and SXDF images. The dotted lines show Gaussian fits with $\sigma = 3.2$ arcsec which were constrained to be centred at $\alpha = \delta = 0$ arcsec.

search radius within which we have hunted for radio counterparts explains why the observed number of counterparts falls below that predicted for a random population in the outermost bins of Fig. 2. Note that Fig. 2 uses *all* the radio identifications, rather than just those with the lowest P values, so any bias present is due only to the finite search radii used to find radio emitters for this analysis (12.5 arcsec).

Having corrected the observed distributions for the expected unrelated 'field' radio sources (those in the background and foreground), a Gaussian fit centred at $\alpha = \delta = 0$ arcsec, shown in Fig. 2, yields a FWHM of 7.5 ± 0.7 arcsec (7.4 ± 0.6 arcsec if the centroid is unconstrained). This translates into $\Delta\alpha = \Delta\delta =$ FWHM/2.354 = 3.2 arcsec. Our correction for the expected 'field' sources should have dealt with any broadening due to radio sources unrelated to the SMGs. The median SNR of the radio-detected sample used in this analysis is 3.0, after correction for Malmquist-type bias, which implies that $\Delta\alpha = \Delta\delta = 0.66\,\theta\,(\text{SNR})^{-1}$, adopting $\theta = 14.5$ arcsec, i.e. 10 per cent higher than expected.

Table 6. Identification summary.

Nickname	Robust identification?	Nickname	Robust identification?
LOCK850.01	● ○	SXDF850.01	●
LOCK850.02	● ○ †	SXDF850.02	● ○
LOCK850.03	● ○ †	SXDF850.03	●
LOCK850.04	● ○ †	SXDF850.04	● ○
LOCK850.05		SXDF850.05	● ○
LOCK850.06	● ○	SXDF850.06	● ○ †
LOCK850.07	● ○	SXDF850.07	● ○
LOCK850.08	○	SXDF850.08	●
LOCK850.09	● ○	SXDF850.09	
LOCK850.10	●	SXDF850.10	●
LOCK850.11		SXDF850.11	● ○
LOCK850.12	● ○	SXDF850.12	●
LOCK850.13		SXDF850.14	●
LOCK850.14		SXDF850.15	
LOCK850.15	● ○ †	SXDF850.16	●
LOCK850.16	● ○	SXDF850.17	
LOCK850.17	● ○	SXDF850.18	●
LOCK850.18	●	SXDF850.19	● ○
LOCK850.19	○	SXDF850.20	
LOCK850.21	○	SXDF850.21	● ○
LOCK850.22	○	SXDF850.22	
LOCK850.23		SXDF850.23	●
LOCK850.24	● ○	SXDF850.24	● ○ †
LOCK850.26	● ○	SXDF850.25	
LOCK850.27		SXDF850.27	● ○
LOCK850.28		SXDF850.28	● ○ †
LOCK850.29	♣	SXDF850.29	● ○
LOCK850.30	● ○	SXDF850.30	● ○
LOCK850.31	● ○	SXDF850.31	● ○
LOCK850.33	●	SXDF850.32	
LOCK850.34	●‡	SXDF850.35	● ○
LOCK850.35		SXDF850.36	
LOCK850.36		SXDF850.37	● ○
LOCK850.37	● ○ ‡	SXDF850.38	●
LOCK850.38	● ○	SXDF850.39	
LOCK850.39		SXDF850.40	●
LOCK850.40	●	SXDF850.45	
LOCK850.41	● ○ †	SXDF850.47	● ○ †
LOCK850.43	○	SXDF850.48	
LOCK850.47		SXDF850.49	
LOCK850.48	○‡	SXDF850.50	●‡
LOCK850.52	● ○	SXDF850.52	● ○ †
LOCK850.53	○	SXDF850.55	●
LOCK850.60		SXDF850.56	
LOCK850.63	● ○	SXDF850.63	
LOCK850.64		SXDF850.65	
LOCK850.66		SXDF850.69	
LOCK850.67	○	SXDF850.70	● ○
LOCK850.70	♣	SXDF850.71	○
LOCK850.71	●	SXDF850.74	●
LOCK850.73	● ○ †	SXDF850.76	
LOCK850.75		SXDF850.77	● ○
LOCK850.76	● ○	SXDF850.86	
LOCK850.77	● ○	SXDF850.88	
LOCK850.78		SXDF850.91	
LOCK850.79	○	SXDF850.93	
LOCK850.81		SXDF850.94	
LOCK850.83	○	SXDF850.95	
LOCK850.87	● ○	SXDF850.96	●
LOCK850.100	♣	SXDF850.119	● ○

● indicates a robust ($P \leqslant 0.05$) radio identification.
○ indicates a robust identification at 24 μm.
♣ coincident radio and 24-μm emission (both $P \leqslant 0.1$) yields reliable identification.
† indicates multiple robust ($P \leqslant 0.05$) identifications.
‡ close visual inspection of the data reveals more than one good identification.

This procedure was replicated for the 24-μm counterparts listed in Tables 3 and 4, correcting for blank-field, background source densities of 4.5 and 1.2 arcmin^{-2} to limits of 50 and 150 μJy, respectively. The result, shown in the right panel of Fig. 2, is a wider distribution, borne out by the best-fit Gaussian: a FWHM of 10.7 ± 1.0 arcsec, when constrained to be centred at $\alpha = \delta = 0$ arcsec, or $\Delta\alpha = \Delta\delta = 4.5$ arcsec. The low accuracy of the 24-μm positions relative to those determined at 1.4 GHz can account for most of the extra width.
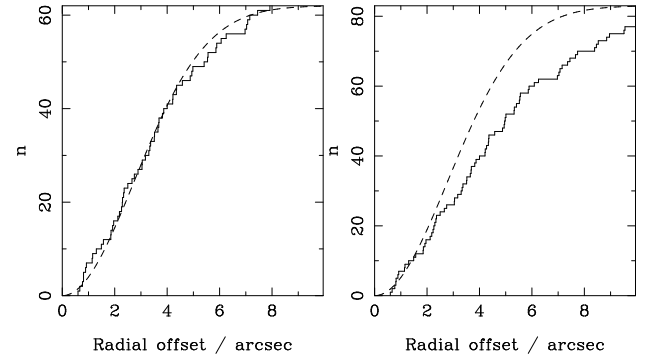
Figure 3. *Left:* Cumulative distribution of radial offsets between the radio and submm positions for the 62 statistically secure ($P \leqslant 0.05$) radio identifications. The dashed line shows the predicted distribution $(1 - e^{-r^2/2\sigma^2})$ assuming that the positional uncertainty in R.A. or Dec. is given by $\sigma = 0.6\,\theta/\mathrm{SNR}$, as discussed in Appendix B, where we have used the mean SNRs for the sample. A KS test yields a probability of 0.57 that the data are consistent with the model. *Right:* The same predicted probability distribution (dashed line), this time compared with the cumulative distribution for all 83 sources with candidate radio identifications (i.e. including those for which $P > 0.05$). The poor fit in the right-hand plot – a KS test yields a probability of 0.0003 that the data are consistent with the model – demonstrates the importance of using the P statistic to filter the candidate list of associations.

As a second way of quantifying this approach, we can consider only the subset of 'robust' radio identifications ($P \leqslant 0.05$) on the basis that this should provide the most secure measure of the true distribution of uncertainty in the submm positions. The radial offset distribution for this subset of 62 sources is shown in the left-hand panel of Fig. 3, where it is compared with the predicted cumulative distribution $(1 - e^{-r^2/2\sigma^2})$, using $\sigma = 0.6\,\theta\,(\mathrm{SNR})^{-1}$ as discussed in Appendix B. For this calculation we have adopted $\theta = 14.5$ arcsec and SNR = 3.17 (the average SNR for the deboosted 850-μm flux densities of these 62 sources). It is clear from this plot that the predicted distribution is in excellent agreement with that observed for this secure subset of identified sources; indeed, a Kolmogorov-Smirnov (KS) test yields a 57-per-cent probability that the data are consistent with the model. For completeness, the right-hand panel in Fig. 3 shows the same predicted probability distribution, this time compared with the cumulative distribution for all 83 sources with candidate radio identifications, i.e. including those for which $P > 0.05$. The same KS test now yields a probability of less than 0.1 per cent. These plots give confidence that the radial offset distribution of secure identifications is consistent with that expected given the JCMT's beam and the deboosted 850-μm flux densities of the SHADES sources and that there is no additional significant source of astrometric error in the submm maps. They also demonstrate the importance of using the P statistic to filter the candidate list of associations for robust identifications.

In conclusion, there is no evidence for significant additional sources of positional error. For an SMG discovered in a submm survey where a Malmquist-type bias correction has not been applied, we can parameterise its positional uncertainty as follows. Its position having been determined after smoothing with the beam, a circle of radius $0.91\,\theta\,(\mathrm{SNR}_{\mathrm{app}}^2 - (2\beta + 4))^{-1/2}$, for power-law counts of the form $N(> f) \propto f^{-\beta}$, has a 68 per cent chance of containing the submm emitter (where $\mathrm{SNR}_{\mathrm{app}}$ is the raw SNR, uncorrected for flux boosting – see Appendix B), or $0.91\,\theta\,(\mathrm{SNR})^{-1}$ if a correction *has* been applied. These correspond to conventional 1-σ error circles.
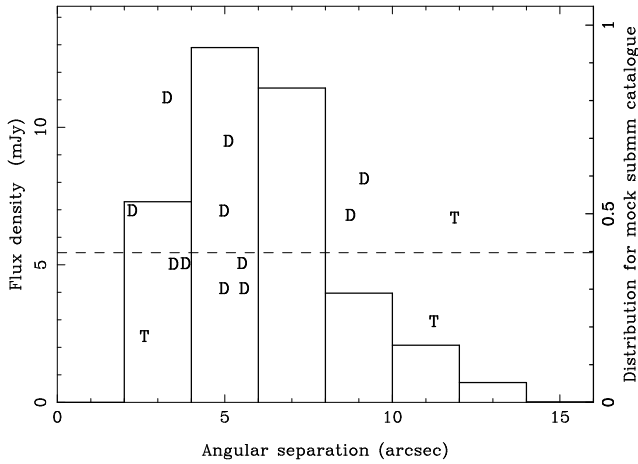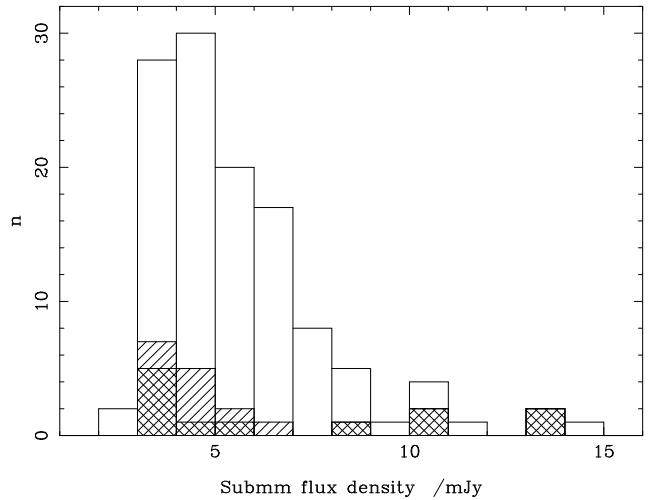
Figure 4. Deboosted submm flux density versus the angular separation of the counterparts for SMGs with more than one robust radio identification ($P \leqslant 0.05$) within 8 arcsec of the 850-μm position. Points denote radio doubles (D) and triples (T). The average of the single, unresolved or barely resolved radio counterparts is represented by a dashed line. The paucity of data at very low and high separations is due to our finite spatial resolution on the one hand and to our use of a finite search area and the P statistic on the other. The histogram shows the distribution of angular separations, scaled arbitrarily, for multiple identifications found in the Monte-Carlo simulations described in §5.

We return now to our initial motivation for this study of positional uncertainty, namely the feasibility of a spectroscopic redshift distribution for SMGs based on KMOS near-IR spectroscopy of an unbiased sample. Such a programme could afford to lose one SMG due to positional error during a single deployment of the 24 KMOS IFUs. Each IFU covers 2.8×2.8-arcsec^2 so, leaving room for seeing effects, we require $2\sigma \sim 2.5$ arcsec to ensure that 95.6 per cent of SMGs fall within the central 5 arcsec^2 of each IFU. Our parameterisation suggests that this level of accuracy requires an SMG sample cut at $\mathrm{SNR} \geqslant 20$. Adopting the source counts of Coppin et al. (2006), a source density of $\sim 2200\,\mathrm{deg}^{-2}$ – sufficient to employ all 24 KMOS IFUs – would require that we probe the 3-mJy SMG population; this, in turn, would require that we delve well below the 850-μm confusion limit to ensure $\mathrm{SNR} \geqslant 20$, or that we utilise positions determined using the 450-μm data that are acquired simultaneously by SCUBA-2. Optimal exploitation of KMOS may require sharing the IFUs with other programmes in all but the deepest SCUBA-2 survey fields.

5   MULTIPLE RADIO COUNTERPARTS

A number of SMGs with more than one robust ($P \leqslant 0.05$) radio counterpart are apparent in Tables 1–2 and Figs A1–A2: seven in the LH and five in the SXDF. This tendency for $\sim$10 per cent of SMGs to have multiple radio identifications was noted previously by Ivison et al. (2002) and Pope et al. (2006). The probability of an SMG possessing two statistically significant radio counterparts was quantified by placing 10^6 fake sources into the real LH and SXDF radio fields and counting the number of $P < 0.05$ radio counterparts – a simple Monte-Carlo approach. This revealed that the calibration of the P statistic is secure, with $P = 0.05$ yielding 5.05 spurious associations for every 100 fake SMGs. Multiple robust counterparts are far rarer, however. For every 100 fake SMGs the simulations suggest that only 0.22 will have more than one secure

Figure 5. Histogram of deboosted submm flux density for the full SHADES Source Catalogue. Cross-hatched areas represent the 12 SMGs with two or more radio components within 8 arcsec of the 850-μm position, associated robustly with the SMG ($P \leqslant 0.05$); single-hatched areas represent the seven SMGs with multiple, significant 24-μm identifications. Five SMGs have multiple, significant radio *and* 24-μm identifications.

radio identification by chance, a figure dominated by doubles, so at first sight the observed tendency for multiple robust radio counterparts is highly significant. However, we know that around half (65) of the SHADES SMGs have a *real* association with a radio emitter, or 59 after accounting for the six spurious identifications we expect (0.05×120), so should we be surprised to find a dozen SMGs with multiple radio identifications? Of the radio-identified SHADES SMGs, 5 per cent will be spuriously associated with another radio source. We thus expect three multiple identifications whereas we see a dozen: a significant difference.

Looking at this another way, the fraction of radio-identified SMGs with multiple radio counterparts is 18.5 ± 5.3 per cent (12/65), 15.4 ± 4.9 per cent (10) with separations below 6 arcsec. How frequent are such cases amongst the general radio population? The proportion of radio sources in the SHADES fields with radio companions within 4, 6, 8 and 10 arcsec are (cumulatively) 1.2 ± 0.3, 3.9 ± 0.5, 7.1 ± 0.6 and 10.3 ± 0.7 per cent (Poisson uncertainties). The number of SMGs with separations below 10 arcsec, and particularly below 6 arcsec, is thus significant. Interestingly, bright SMGs make up one in seven of all radio multiples with separations below 6 arcsec.

What causes this multiplicity? At least three mechanisms could be responsible: AGN-driven jets; physical interactions; and confusion.

Discriminating between these mechanisms is extremely difficult. The first – jets – could be revealed via their morphology or their radio spectral index, but to date neither property has been probed for a significant sample. The spectroscopic evidence required to reveal the second possibility – a physical association – is available only rarely in the SHADES fields, although a number of linked, multiple systems with few-arcsec separations and near-identical redshifts have been documented elsewhere (Ivison et al. 1998, 2000; Ledlow et al. 2002; Neri et al. 2003; Smail et al. 2003a; Chapman et al. 2005; Tacconi et al. 2006) which leaves little doubt that many SMGs with multiple radio identifications are interaction-driven starbursts with separations of ten (or a few tens) of kpc.

Fig. 4 shows a plot of submm flux density versus angular sep-
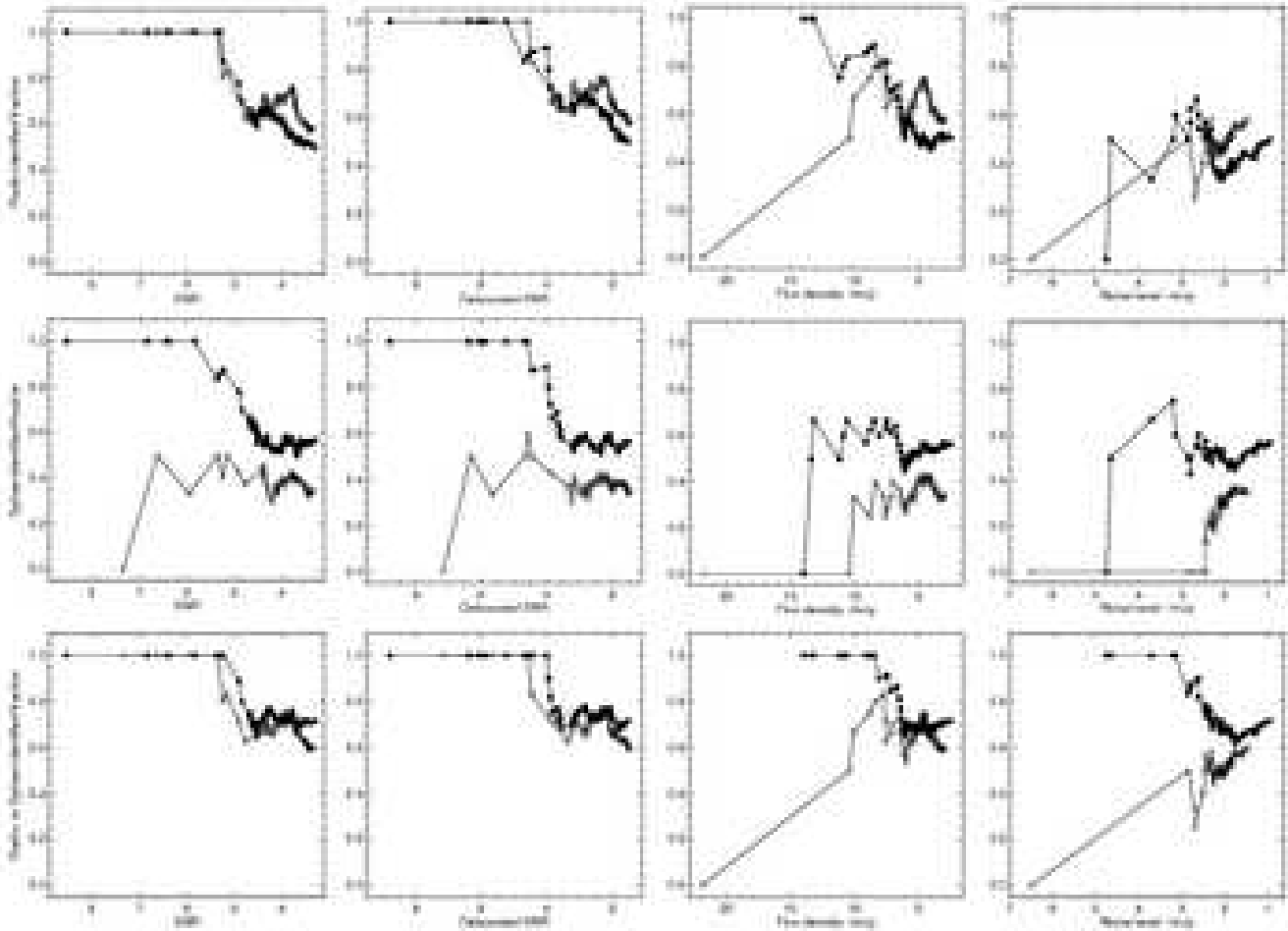
Figure 6. *Top row:* from left to right, plots of the cumulative radio-identified fraction for the LH SMG sample (filled circles) and the SXDF SMG sample (open circles) against submm SNR *before* flux deboosting, submm SNR *after* deboosting, 850-μm flux density *after* deboosting and 850-μm noise level. *Middle row:* the same plots, but for source identification at 24 μm. *Bottom row:* the same plots, allowing for identifications at 24 μm, 1.4 GHz, or coincident weak emission at both as summarised in Table 6.

aration for those SHADES SMGs with more than one radio counterpart and we see no contradiction of the previous trend: two thirds of the multiple identifications have separations of 2–6 arcsec. However, our data and our approach bias us against finding systems with smaller and larger separations, as can be seen by the distribution of separations found for fake SMGs with multiple radio counterparts during our Monte-Carlo simulations (Fig. 4). High-resolution radio imaging from MERLIN has provided examples of multiple, discrete radio sources separated by 0.2–2 arcsec (Chapman et al. 2004; Biggs et al., in preparation), though they are rare.

The size of the SHADES survey provides a unique opportunity to probe the third mechanism – confusion. The steepness of the submm counts may yield examples where two or more faint, unrelated SMGs share a sightline and thus conspire to create a seemingly bright SMG. There is approximately one SMG in the $2 < S_{850\mu m} < 4$ mJy flux density range for every 4.3 arcmin^2 of sky, according to the differential counts presented by Coppin et al. (2006). We thus expect 185 ± 50 such sources in the SHADES fields. The probability of a 2–4-mJy SMG lying within 7 arcsec of another source is $\sim$1 per cent, so we could expect to see two of these amalgamated sources at flux densities between 4 and 8 mJy in the SHADES sample. This flux density range accounts for 62.5

per cent of the full sample, so we might expect around three such sources in total (perhaps rather more if we included amalgamations of far more common, fainter sources). Of these three, two should have a real radio identification; one may have several. The difficulty we face in exploring this small subset of amalgamated sources is in knowing which of the SHADES SMGs they are. One prediction might be that they are expected to have fainter counterparts at other wavelengths, but even this may be premature (Serjeant et al. 2007). We must content ourselves with the knowledge that they should be revealed via SCUBA-2 450-μm imaging in the near future.

Without spectroscopic data we cannot determine whether physical interactions or confusion make up the majority of the SMGs with multiple identifications, let alone whether bright SMGs are special cases where two massive components are merging, as suggested by Smail et al. (2003b). The median deboosted submm flux density of the SHADES Source Catalogue is 5.0 mJy; the error-weighted mean 850-μm flux density of SMGs with more than one radio counterpart is 5.8 ± 0.4 mJy; that for a comparison sample, the 48 SMGs with a single $P \leqslant 0.05$ radio counterpart, is 5.4 ± 0.2 mJy, so the simplest approach yields no evidence of a difference between SMGs with single and multiple identifications. Fig. 5 shows the distribution of deboosted submm flux density for

the whole SHADES Source Catalogue and for those sources with multiple robust counterparts at 1.4 GHz or 24 μm. Taking the median SHADES flux density as our threshold, eight multiple identifications lie above and 11 lie below, respectively (six apiece using only the radio). However, as our flux density threshold rises to 10 mJy so the fraction of sources with multiple identifications rises from 15/111 to 4/9 (or 8/111 to 4/9 using only the radio); even ignoring the high probability that one of the remaining five bright sources may be spurious (SXDF850.45) and that another has several possible counterparts (Lock850.34 – Table 6), this is a significant trend. It is plausible that these sources are examples of confusion (i.e. amalgamated sources) but we note that the physically linked systems reported to date are often similarly bright.

We conclude that the incidence of very high flux density and counterpart multiplicity are weakly linked and that the case for a preferred separation between multiple counterparts is plausible but not proven. In particular, we note that almost half of the brightest nine SMGs – all >10 mJy – have multiple radio counterparts and that all have separations in the range 2–6 arcsec, or 20–70 kpc at their likely redshifts and at an inclination of $45°$ to the sky, perhaps enabling efficient gas fueling for central starbursts or AGN via overlapping galactic disks — see the qualitative discussion and illustrations (particularly Figs 11–13) in the merger simulations of Springel, Di Matteo, & Hernquist (2005) where a particularly intense burst of activity occurs on first passage for systems that lack prominent bulges, with galaxy separations of ∼30 kpc for the subsequent few tens of Myr.

6   RADIO AND MID-IR IDENTIFICATION TRENDS AND SUBMM SAMPLE REFINEMENT

Following Ivison et al. (2002), we seek to exploit the clear prediction that spurious SMGs will lack radio or mid-IR counterparts. Genuine sources can, of course, evade radio or mid-IR detection – because they lie at extreme redshift, for example (see Ivison et al. 2005) – but general trends in the identification rate may be evident. In this section we therefore explore what can be learned about the SMGs without counterparts.

Fig. 6 shows the cumulative identification rate for SMGs in the LH and SXDF fields as a function of submm SNR (before and after flux deboosting), deboosted submm flux density and submm flux uncertainty.

6.1   Radio trends

Looking at the radio identification trends as functions of submm flux density and noise, we see the recovery rate tailing off at the faintest flux density limits (<5 mJy) in SXDF, whereas the rate is remarkably flat for fainter flux densities in the LH field. Both fields show improving identification rates as the submm noise declines, despite the deboosting procedures outlined in Paper II – a worrying trend, though we should bear in mind that searching for identifications within a fixed radius must act as a bias against low-SNR sources. For the highest values of submm flux density and noise we see similarities with trends discussed by Ivison et al. (2002) for the 8-mJy Survey, i.e. the brightest source in each field lies in a region with high noise, and neither has a robust radio counterpart.

The SXDF radio identification rate versus raw submm SNR shows a steep decline below an SNR of 4; after flux deboosting this effect is mitigated somewhat, with matching trends in the SXDF and LH fields. It is noteworthy that the overall radio recovery rate

in SXDF is over 10 per cent higher than in the LH field, despite the shallower depth of the SXDF radio imaging. We attribute this to three effects, each of which we believe contributes to the unexpectedly low LH identification rate: first, the LH radio image is a single pointing, designed originally to identify SMGs in the small 8-mJy Survey field (cf. a mosaic of three in SXDF), so the pernicious effect of bandwidth smearing will be evident for a significantly larger fraction of the SHADES field in LH than in SXDF; second, although it is clearly useful to work with the best possible radio data, deep imaging inevitably yields more faint, unrelated, background sources, causing P values for relatively bright counterparts to rise relative to those calculated for a lower source density; third, it is possible (though it has yet to be shown unambiguously – Ivison et al. 2002; Chapman et al. 2004; Muxlow et al. 2005) that a significant fraction of the emission in some SMGs is resolved by high-resolution radio data. That these effects are significant, collectively, is demonstrated by the significantly higher SMG identification rate in the shallower, lower resolution SXDF data; in addition, seven LH SMGs (LOCK850.10, .34, .37, .38, .40, .77 and .100) are detected robustly only in the noisier, low-resolution radio image, though we note that in several cases the 4.2-arcsec FWHM image alone does not allow us to differentiate between plausible spectroscopic targets. There are several lessons here: ensure interferometric data contain an adequate fraction of short spacings – a synthesised beam with 1.5–2 arcsec FWHM provides a good compromise for identification of FIR-luminous galaxies; where necessary, i.e. when the area of interest is similar to that of the radio interferometer's primary beam and the spectral resolution is poor ($\delta\lambda/\lambda < 1000$), obtain data in a compact mosaic of pointings rather than a single, deep pointing.
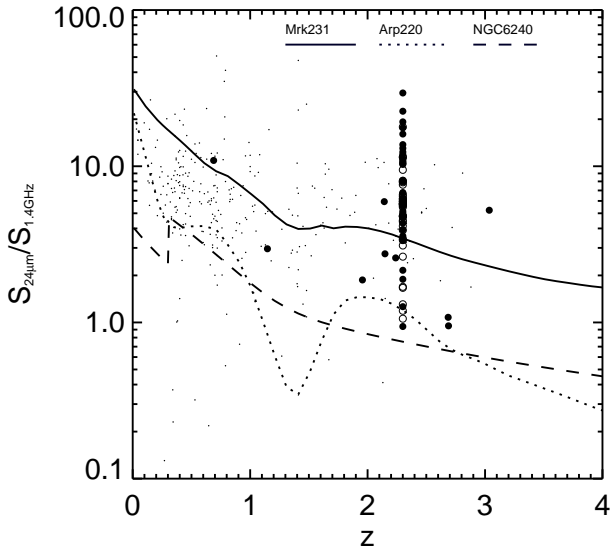
6.2   Mid-IR trends

The trend of overall recovery rate is reversed in the mid-IR, the LH yielding a 20 per cent higher identification rate than the SXDF. The reason is obvious, however: it is due to the substantial extra depth of the LH *Spitzer* 24-μm data ($\sigma = 11$ versus 47 μJy). Only one SMG is identified solely on the basis of its mid-IR emission in SXDF compared with ten in the LH. For both fields the decline at low deboosted SNR is less marked than the radio trend. Against submm flux density and noise, the 24-μm identification trends for both fields match those at radio wavelengths (with the aforementioned 20 per cent offset for the SXDF sources); the very brightest sources again lack robust counterparts.

6.3   Overall trends

The lower row of plots in Fig. 6 show the *overall* identification trends – the fraction of sources identified at 1.4 GHz and/or 24 μm, including the three cases mentioned in §3 where weak radio and 24-μm counterparts are coincident (one of which is the brightest LH source, LOCK850.34).

The identification trends are similar for the two SHADES fields: identification is essentially complete above a deboosted submm SNR of ∼4 with an abrupt step down to 60–70 per cent thereafter; also, success rates improve as the submm noise declines. The SXDF identification rate tails off below a deboosted submm SNR of 2.5 and at submm flux densities below 5 mJy. This may be due to the limited depth of the SXDF radio and 24-μm imaging rather than any deficiency of the SXDF catalogue, but we note that it is a strong tendency.

7 CONSTRAINTS FROM SPECTRAL INDICES

7.1 $S_{24\mu m}/S_{1.4GHz}$

Since the spectral slopes at 24 μm and 1.4 GHz are similar, it may prove instructive to examine the behaviour of $S_{24\mu m}/S_{1.4GHz}$ as a function of redshift, as shown in Fig. 7. We expect this plot to betray AGN contributions to the radio flux density in so-called 'radio-excess AGN' (Drake et al. 2003; Donley et al. 2005) or, conversely, 'mid-IR-excess AGN' which have QSO-heated dust but little or no AGN-related emission in the radio. For star-forming galaxies this ratio is tightly constrained out to $z = 1$ (Appleton et al. 2004). Galaxies with low values of $S_{24\mu m}/S_{1.4GHz}$, i.e. those with strong radio with respect to 24-μm emission, are unlikely to be dominated by star formation.

The SHADES SMGs share approximately the same distribution of $S_{24\mu m}/S_{1.4GHz}$ values as the other radio sources in SXDF (Ibar et al., in preparation). Fig. 7 shows the redshift tracks of Arp 220, NGC 6240 and Mrk 231 – archetypal ultraluminous IR galaxies with increasing degrees of AGN contribution. Measured values of $S_{24\mu m}/S_{1.4GHz}$ for the SHADES SMGs are consistent with any of these SEDs but Mrk 231 is the preferred template, implying an AGN contribution to the mid-IR luminosity. Only at $z < 1$ could the most extreme SMG be classified confidently as having a radio excess.

7.2 $S_{850\mu m}/S_{1.4GHz}$

Hughes et al. (1998) and Carilli & Yun (1999) pointed out the value of $S_{850\mu m}/S_{1.4GHz}$ as an indicator of redshift for SMGs, at least for $z < 3$. Smail et al. (2000) and Ivison et al. (2002) were the first to employ the technique for significant samples of SMGs, finding median redshifts, $z \gtrsim 2$.

Chapman et al. (2005) found that the relation showed a large dispersion for their sample of radio-identified SMGs with spectroscopic redshifts, indicative of a range of SEDs. They noted that a purely submm-selected sample should show an even wider range of $S_{850\mu m}/S_{1.4GHz}$ than their radio-identified SMGs, since the need for an accurate radio position biases the sample in redshift and temperature.

The surprisingly flat trend identified by Chapman et al., uncorrected for a probable redshift-dependent ~ 0.3 dex shift attributable to their radio selection criteria, was parameterised as $S_{850\mu m}/S_{1.4GHz} = 11.1 + 35.2\,z$. This parameterisation was not intended as a careful photometric redshift technique – the r.m.s. scatter in redshift is ~ 1, after all – but likely remains the best way to estimate the median redshift of radio-identified SMG samples. Applying this to our sample of 65 SMGs with robust radio counterparts yields a median redshift of 2.8, with an interquartile range of 1.3–3.8, somewhat higher and broader than the spectroscopic redshift distribution reported by Chapman et al. (median $z = 2.2$, interquartile 1.7–2.8, before their small correction for the radio selection function). The Chapman et al. parameterisation is not appropriate for SMGs without radio identifications, but for the entire SHADES sample (adopting the limits in Tables 1–2 for those lacking formal detections) it indicates a median redshift of 3.3.

The difference between the distribution reported here and that of Chapman et al. (2005) is quite marked, but can be explained by a variety of effects: spectroscopic bias; field-to-field variations; strong clustering of the SMG population (Blain et al. 2004); our adoption of deboosted flux densities for all SHADES sources (a large proportion of the Chapman et al. sample is likely to have suffered a submm flux density boost of one form or another); and, not

Figure 7. Ratio of $S_{24\mu m}/S_{1.4GHz}$ as a function of redshift, z, for SHADES sources with robust counterparts (filled circles: LH; empty circles: SXDF). Those without spectroscopic redshifts – the majority – are plotted arbitrarily at $z = 2.3$. The tracks of Arp 220, Mrk 231 and NGC 6240 are shown together with a sample of faint radio sources in SXDF (small dots – Ibar et al., in preparation).
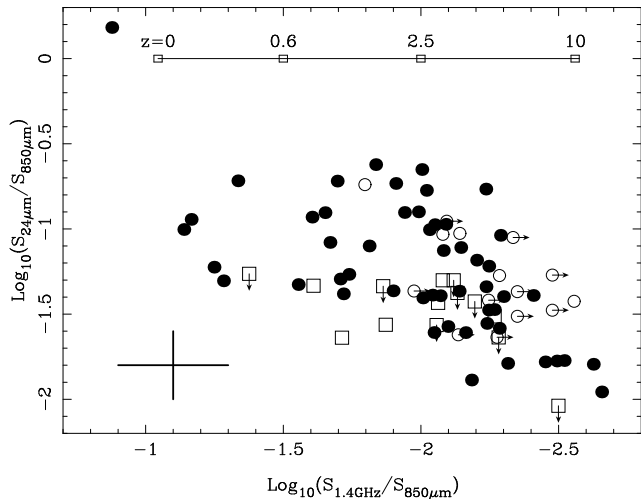
Figure 8. $\mathrm{Log}_{10}\,S_{24\mu m}/S_{850\mu m}$ versus $\log_{10}\,S_{1.4GHz}/S_{850\mu m}$ for SHADES SMGs with both mid-IR and radio identifications (filled circles), with only radio identifications (squares) and with only mid-IR identifications (open circles). A representative error bar is shown, lower left. The redshift parameterisation of Chapman et al. (2005) is shown as a horizontal bar at $\log_{10}\,S_{24\mu m}/S_{850\mu m} = 0$ (see §7.2).

Summarising these plots, the best available complementary data in the LH – equivalent to those available in the Great Observatories Origins Deep Survey (GOODS) northern field – allows us to identify robustly over two thirds of SMGs to current submm detection limits. The observed trends in identification rate give no strong rationale for rejecting any sources from the parent SHADES Source Catalogue, although a slight question mark is thrown over some of the lowest SNR sources.

least, the difficulty of measuring accurate and consistent radio flux densities using data with different uv coverage.

Fig. 8 shows a log–log plot of $S_{24\mu m}/S_{850\mu m}$ versus $S_{1.4GHz}/S_{850\mu m}$ for SHADES SMGs, with different symbols representing identifications made in different wavebands (radio plus mid-IR; mid-IR only; radio only). As we have discussed, $S_{1.4GHz}/S_{850\mu m}$ is sensitive to redshift (and temperature) and the Chapman et al. parameterisation is shown as a horizontal bar. It is apparent that 24-μm flux density is correlated significantly with redshift, as expected for the K correction at that wavelength. The SMG with $S_{1.4GHz}/S_{850\mu m} > 0.1$ is SXDF850.21, the most obvious example of a local galaxy in the sample ($z = 0.044$, Simpson et al. 2006; see Appendix A, Fig. A2).

8 THE DIAGNOSTIC POWER OF MID-IR COLOUR

Ivison et al. (2004) used a colour-colour plot to exploit the strong diagnostic potential of the mid-IR for discriminating between galaxies dominated by starbursts and AGN. Key spectral indices for high-redshift galaxies are available between 3.6 and 24 μm since the rest-frame $\sim$3–10 μm slope for starbursts is steeper than for AGN, with a flatter region between 1 and 3 μm, whereas AGN exhibit power-law spectra covering rest-frame $\sim$0.2–10 μm (e.g. Mrk 231).

Fig. 9 shows $S_{24\mu m}/S_{8\mu m}$ versus $S_{8\mu m}/S_{4.5\mu m}$. We expect the low-$S_{8\mu m}/S_{4.5\mu m}$ portion – the left side – to be occupied by $z \gtrsim 0.7$ starbursts, represented here by the redshift track of Arp 220. High-redshift starbursts are expected in the lower left region of Fig. 9, but spectral features in Arp 220's SED yield several kinks which limit the diagnostic power of the plot; power-law AGN, represented in Fig. 9 by Mrk 231, track left-to-right with increasing redshift across the lower third of the plot, returning to the left only $z \gtrsim 4$. The redshift track of NGC 6240 – a classical Compton-thick AGN displaying mid-IR PAH features indistinguishable from those of a starburst galaxy – overlaps significantly with the colour-colour space occupied by Arp 220, at $z \sim 0.4$ and at much higher redshifts, but most of the confusing overlap occurs where we expect NGC 6240-type SEDs at $z \sim 0.6$ and Mrk 231-like SEDs at $z > 6$.

Do SMGs stand out from a 24-μm-selected *Spitzer* sample in colour-colour space? Fig. 9 shows an independent galaxy sample selected at 24 μm in the LH, at depths commensurate with our *Spitzer* identifications, and we can see that the data are clustered along the track occupied by Arp 220-like SEDs for $z \geqslant 0.7$, with a significant number of sources along the track defined by a Mrk 231-like SED. SMGs are similarly positioned and do not stand out clearly from 24-μm-selected galaxies. However, the hatched areas of Fig. 9 – those colour combinations where we might expect to find SMGs with the highest redshifts ($z \gtrsim 4$) – are well populated with SMGs. The fraction of SMGs in these regions is significantly larger than for the control sample: we find only 14 per cent of the 4,457 mid-IR-selected galaxies in the hatched regions. Based on the Chapman et al. parameterisation of $S_{850\mu m}/S_{1.4GHz}$, their median redshift is higher than that of the radio-detected fraction of SHADES, 3.2 versus 2.8, although we note that some of the best $z \lesssim 1$ candidates also fall in these regions, e.g. SXDF850.52. Nevertheless, it seems sensible that any search for a high-redshift population of SMGs should base its target selection on a combination of the $S_{850\mu m}/S_{1.4GHz}$, $S_{1200\mu m}/S_{850\mu m}$ (Eales et al. 2003; Greve et al. 2004), $S_{24\mu m}/S_{8\mu m}$ and $S_{8\mu m}/S_{4.5\mu m}$ colours.

9 CONCLUDING REMARKS

We have determined the most likely radio and/or mid-IR identifications, and hence accurate positions, for the SHADES Source Catalogue presented by Coppin et al. (2006). We have identified robust counterparts to over two thirds of this sample (54 and 46 per cent at 1.4 GHz and 24 μm, respectively), presenting optical, 24-μm and radio images of each SMG.

Employing the submm/radio flux density ratio as an indicator of redshift, guided by the Chapman et al. (2005) parameterisation, we find a median redshift of 2.8 for the radio-identified sample, somewhat higher than the spectroscopic median.

We present a diagnostic colour-colour plot, based on *Spitzer* data, in which we identify regions commensurate with SMGs at very high redshift.

We further exploit our identifications to show that:

- observed trends in identification rate give no strong rationale for pruning the parent SHADES sample (cf. Ivison et al. 2002);
- uncertainties in submm position are consistent with theoretical expectations, with no evidence for significant additional sources of positional error;
- significantly more SMGs have multiple robust counterparts than would be expected by chance, indicative of physical associations. These multiple systems are most common amongst the brightest SMGs and are typically separated by 2–6 arcsec, $\sim$15–50/sin i kpc at $z \sim 2$, consistent with early bursts seen in merger simulations.

References

Alexander D.A., Bauer F.E., Chapman S.C., Smail I., Blain A.W., Brandt W.N., Ivison R.J., 2005a, ApJ, 632, 736
Alexander D.A., Smail I., Bauer F.E., Chapman S.C., Blain A.W., Brandt W.N., Ivison R.J., 2005b, Nature, 434, 738
Aretxaga I. et al., 2007, MNRAS, submitted (astro-ph/0702503)
Ashby M.L.N. et al., 2006, ApJ, 644, 778
Barger A.J., Cowie L.L., Sanders D.B., Fulton E., Taniguchi Y., Sato Y., Kawara K., Okuda H., 1998, Nature, 394, 248
Barger A.J., Cowie L.L., Smail I., Ivison R.J., Blain A.W., Kneib J.-P., 1999, AJ, 117, 2656
Barger A.J., Cowie L.L., Richards E.A., 2000, AJ, 119, 2092
Bertoldi F. et al., 2000, A&A, 360, 92
Biggs A.D., Ivison R.J., 2006, MNRAS, 371, 963
Binney J., Merrifield M., 1998, *Galactic Astronomy*, Princeton
Blain A.W., Ivison R.J., Smail I., 1998, MNRAS, 296, L29
Blain A.W., Kneib J.-P., Ivison R.J., Smail I., 1999, ApJ, 512, L87
Blain A.W., Chapman S.C., Smail I., Ivison R.J., 2004, ApJ, 611, 725
Bond J.R., Efstathiou G., 1987, MNRAS, 226, 655
Borys C., Chapman S., Halpern M., Scott D., 2003, MNRAS, 344, 385
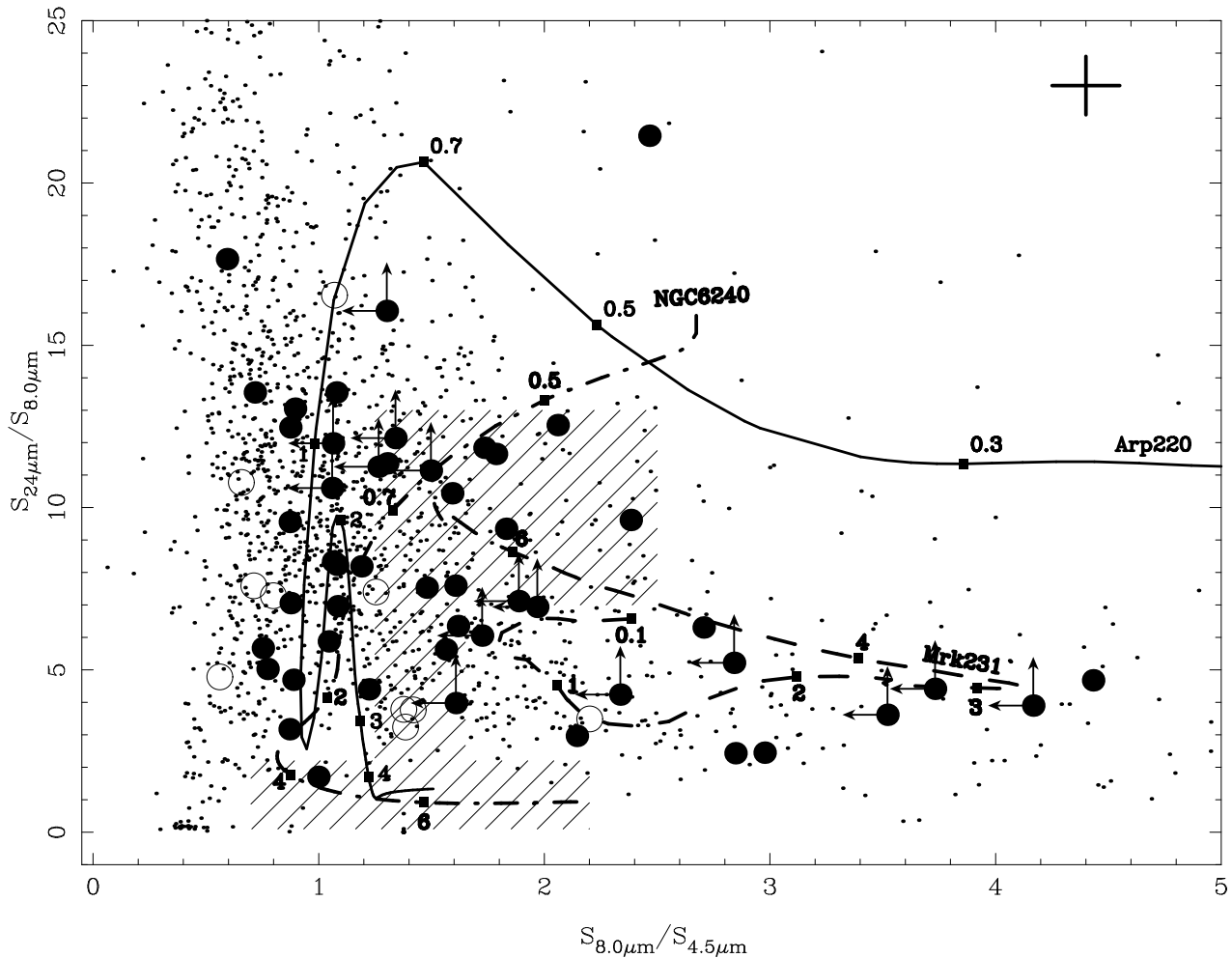
Figure 9. $S_{24\mu m}/S_{8\mu m}$ versus $S_{8\mu m}/S_{4.5\mu m}$ colour-colour diagram for a faint 24-μm-selected sample of 4,457 galaxies (dots) with 4.5- and 8.0-μm detections. Robustly identified SMGs are plotted as filled circles and less securely identified SMGs as open circles. A representative error bar is shown, top right. The redshift tracks of Arp 220, Mrk 231 and NGC 6240 are shown (adopting SEDs from Rigopoulou et al. 1999 and Spoon et al. 2004), with squares to indicate redshift. Hatched regions indicate regions of colour-colour space where one might expect to find the most distant SMGs.

Borys C., Scott D., Chapman S., Halpern M., Nandra K., Pope A., 2004, MNRAS, 355, 485

Carilli C.L., Yun M.S., 1999, ApJ, 513, L13

Carilli C.L., Yun M.S., 2000, ApJ, 530, 618

Chapman S.C., Lewis G.F., Scott D., Borys C., Richards E.A., 2002, ApJ, 570, 557

Chapman S.C., Blain A.W., Ivison R.J., Smail I., 2003, Nature, 422, 695

Chapman S.C., Smail I., Windhorst R., Muxlow T., Ivison R.J., 2004, ApJ, 611, 732

Chapman S.C., Blain A.W., Smail I., Ivison R.J., 2005, ApJ, 622, 772

Clements D. et al., 2004, MNRAS, 351, 611

Condon J.J., 1997, PASP, 109, 166

Coppin K., Halpern M., Scott D., Borys C., Chapman S., 2005, MNRAS, 357, 1022

Coppin K. et al., 2006, MNRAS, 372, 1621 (Paper II)

Dannerbauer H., Lehnert M.D., Lutz D., Tacconi L., Bertoldi F., Carilli C., Genzel R., Menten K.M., 2004, ApJ, 606, 664

Donley J.L., Rieke G.H., Rigby J.R., Pérez-González P.G., 2005, ApJ, 634, 169

Downes A.J.B., Peacock J.A., Savage A., Carrie D.R., 1986, MN-

RAS, 218, 31

Drake C.L., McGregor P.J., Dopita M.A., van Breugel W.J.M., 2003, AJ, 126, 2237

Duncan W.D., Sandell G., Robson E.I., Ade P.A.R., Griffin M.J., 1990, MNRAS, 243, 126

Dunlop J.S., Peacock J.A., Savage A., Lilly S.J., Heasley J.N., Simon A.J.B., 1989, MNRAS, 238, 1171

Dunlop J.S. et al., 2004, MNRAS, 350, 769

Dunne L., Clements D.L., Eales S.A., 2000, MNRAS, 319, 813

Eales S.A, Lilly S.J., Gear W.K., Dunne L., Bond J.R., Hammer F., Le Fèvre O., Crampton D., 1999, ApJ, 515, 518

Eales S., Lilly S., Webb T., Dunne L., Gear W., Clements D., Yun M., 2000, AJ, 120, 2244

Eales S., Bertoldi F., Ivison R.J., Carilli C., Dunne L., Owen F., 2003, MNRAS, 344, 169

Egami E. et al., 2004, ApJS, 154, 130

Fox M.J. et al., 2002, MNRAS, 331, 839

Frayer D.T., Ivison R.J., Scoville N.Z., Yun M., Evans A.S., Smail I., Blain A.W., Kneib J.-P., 1998, ApJ, 506, L7

Frayer D.T. et al., 1999, ApJ, 514, L13

Frayer D.T. et al., 2004, ApJS, 154, 137

Gear W.K., Lilly S.J., Stevens J.A., Clements D.L., Webb T.M.,

Eales S.A., Dunne L., 2000, MNRAS, 316, L51

Garrett M.A., Knudsen K.K., van der Werf P.P., 2005, A&A, 431 L21

Greve T.R., Ivison R.J., Bertoldi F., Stevens J.A., Lutz D., Dunlop J.S., 2004, MNRAS, 354, 779

Greve T.R. et al. 2005, MNRAS, 359, 1165

Holland W.S. et al., 1999, MNRAS, 303, 659

Holland W.S., Duncan W., Kelly B.D., Irwin K.D., Walton A.J., Ade P.A.R., Robson E.I., 2003, SPIE, 4855, 1

Hughes D.H. et al., 1998, Nature, 394, 241

Ivison R.J., Smail I., Le Borgne J.-F., Blain A.W., Kneib J.-P., Bézecourt J., Kerr T.H., Davies J.K., 1998, MNRAS, 298, 583

Ivison R.J., Smail I., Barger A., Kneib J.-P., Blain A.W., Owen F.N., Kerr T.H., Cowie L.L., 2000, MNRAS, 315, 209

Ivison R.J. et al., 2002, MNRAS, 337, 1

Ivison R.J. et al., 2004, ApJS, 154, 124

Ivison R.J. et al., 2005, MNRAS, 364, 1025

Knudsen K.K., van der Werf P.P., Jaffe W., 2003, A&A, 411, 343

Kreysa E. et al., 1998, SPIE, 3357, 319

Kreysa E. et al., 2003, SPIE, 4855, 41

Laurent G.T. et al., 2005, ApJ, 623, 742

Ledlow M.J., Smail I., Owen F.N., Keel W.C., Ivison R.J., Morrison G.E., 2002, ApJ, 577, L79

Lonsdale C.J. et al., 2003, PASP, 115, 897

Lutz D. et al., 2001, A&A, 378, L70

Moore G.E., 1965, Electronics, 38, 8, April 19

Mortier A.M.J. et al., 2005, MNRAS, 363, 563 (Paper I)

Muxlow T.W.B. et al., 2005, MNRAS, 358, 1159

Neri R. et al., 2003, A&A, 597, L113

Owen F.N., Keel W.C., Ledlow M.J., Morrison G.E., Windhorst R.A., 2005, AJ, 129, 26

Peacock J.A., 1999, Cosmological physics, Cambridge University Press

Pope A., Borys C., Scott D., Conselice C., Dickinson M., Mobasher B., 2005, MNRAS, 358, 149

Pope A. et al., 2006, MNRAS, 370, 1185

Rengarajan T.N., Takeuchi T.T., 2001, PASJ, 53, 433

Rieke G.H. et al., 2004, ApJS, 154, 25

Rigopoulou D., Spoon H.W.W., Genzel R., Lutz D., Moorwood A.F.M., Tran Q.D., 1999, AJ, 118, 2625

Scott S.E. et al., 2002, MNRAS, 331, 817

Serjeant S. et al., 2004, ApJS, 154, 118

Sharples R.M. et al., 2006, SPIE, 6269, 44

Simpson C., Dunlop J.S., Eales S.A., Ivison R.J., Scott S.E., Lilly S.J., Webb T.M.A., 2004. MNRAS, 353, 179

Simpson C. et al. 2006, MNRAS, 372, 741

Smail I., Ivison R.J., Blain A.W., 1997, ApJ, 490, L5

Smail I., Ivison R.J., Owen F.N., Blain A.W., Kneib J.-P., 2000, ApJ, 528, 612

Smail I., Chapman S.C., Ivison R.J., Blain A.W., Takata T., Heckman T.M., Dunlop J.S., Sekiguchi K., 2003a, MNRAS, 342, 1185

Smail I., Scharf C.A., Ivison R.J., Stevens J.A., Bower R.G., Dunlop J.S., 2003b, ApJ, 599, 86

Spergel D.N. et al., 2003, ApJS, 148, 175

Spoon H.W.W., Moorwood A.F.M., Lutz D., Tielens A.G.G.M., Siebenmorgen R., Keane J.V., 2004, A&A, 414, 873

Springel V., Di Matteo T., Hernquist L., 2005, MNRAS, 361, 776

Springel V. et al., 2005, Nature, 435, 629

Stevens J.A. et al., 2003, Nature, 425, 264

Swinbank A.M., Smail I., Chapman S.C., Blain A.W., Ivison R.J., Keel W.C., 2004, ApJ, 617, 64

Tacconi L. et al., 2006, ApJ, 640, 228

Voss H., Bertoldi F., Carilli C., Owen F.N., Lutz D., Holdaway M., Ledlow M., Menten K.M., 2006, A&A, 448, 823

Webb T.M. et al., 2003a, ApJ, 587, 41

Webb T.M.A., Lilly S.J., Clements D.L., Eales S., Yun M., Brodwin M., Dunne L., Gear W.K., 2003b, ApJ, 597, 680

Werner M.W. et al. 2004, ApJS, 154, 1

Whittet D.C.B., 1992, *Dust in the Galactic Environment*, Cambridge

APPENDIX A: POSTAGE STAMP IMAGES

This section presents 25×25-arcsec postage stamp images of each SMG in the SHADES Source Catalogue as well as a description of the most unusual examples.

Figs A1 and A2 show greyscale R-band optical data in the left-hand panels, where available, and greyscale 24-μm data in the right-hand panels. Superimposed on the R-band images are high-resolution (1.3 arcsec FWHM for the LH, 1.7 arcsec FWHM for SXDF) radio contours, plotted at $-3, 3, 4 \ldots 10, 20 \ldots 100 \times \sigma$, where σ was measured in source-free regions around each SMG and is quoted in the lower-right corner of each image in units of μJy beam^{-1}. Superimposed on the 24-μm data are low-resolution (4.2 arcsec, FWHM) radio contours, plotted at $-3, 3, 4 \ldots 10, 20 \ldots 100 \times \sigma$, where σ was measured in source-free regions around each SMG and is again quoted in the lower-right corner of each image. Broken crosses mark the positions of all 24-μm sources brighter than 150 μJy found within 15 arcsec of SMG positions in SXDF – their positions are listed in Table 4. The large central circles indicate 2σ positional uncertainties where $\sigma = 0.6\,\theta/\text{SNR}$ and de-boosted SNR values have been adopted (Coppin et al. 2006). As shown in §4, there is an 86.5 per cent probability that these circles contain the source of submm emission. For counterpart identification we simply use a radius of 8 arcsec (or 12.5 arcsec for the radio, 15 arcsec at 24 μm, to be more complete).

Solid boxes indicate robust identifications, where $P \leqslant 0.05$ based on the radio or 24-μm counts, or a combination of the two. Dashed boxes indicate tentative associations.

Cases worthy of comment

Some of the SMGs present unusual combinations of observed characteristics and we comment on them here.

LOCK850.06: Betrayed at both 24 μm and 1.4 GHz, but invisible optically.

LOCK850.07: As LOCK850.06, though with an optical counterpart within 1 arcsec; possibly typical of the composite blue-red pairs noted by Ivison et al. (2002).

LOCK850.08: An optical counterpart likely lies behind the diffraction spike. An ideal target for adaptive-optics- (AO-) assisted studies, exploiting the bright star to the north.

LOCK850.11: This apparently obvious 24-μm identification just fails to qualify as a 'robust' counterpart because it comprises two fainter sources. We view these as likely counterparts. They are co-incident with a disturbed optical galaxy which should be targeted spectroscopically.

LOCK850.14: The nearest radio emitter does not qualify as a robust identification but has an excellent spectroscopic redshift in the catalogue of Chapman et al. (2005).

LOCK850.15: A complex system with as many as three plausible identifications, suggestive of a colossal merger.

LOCK850.16: Described in detail by Ivison et al. (2002, 2005).

LOCK850.18: An obvious – though faint – radio identification, yet there is no sign of 24-μm or optical emission.

LOCK850.19: A straightforward 24-μm identification with support from faint radio emission.

LOCK850.21: A solid 24-μm identification; 24-μm and distorted optical emission to the south-east may be related physically.

LOCK850.23: Faint 24-μm and radio emission point to a faint optical counterpart (circled in Fig. A1); well worth targeting spectroscopically, though not formally a robust identification.

LOCK850.29: Faint radio and 24-μm emission yield a formal identification; the double optical galaxy seems to be offset to the north east and yet it resembles many SMGs; it should be targeted spectroscopically.

LOCK850.30: A multiple radio identification. The weakest radio component remains stubbornly above $P = 0.05$; the brightest radio emitter was reported by Ivison et al. (2002) to have an inverted radio spectrum (see Bertoldi et al. 2000 for other examples of this phenomenon). The 24-μm emission appears to lie between the radio components. In one obvious interpretation the radio emission may emanate from lobes powered by a central, black hole- and star-forming galaxy.

LOCK850.34: A multitude of multiple counterparts. An opportunity for detailed study of a potentially complex, interacting system.

LOCK850.37: Robust but distinct identifications at 24 μm and 1.4 GHz. Challenging, optically.

LOCK850.48: A seemingly straightforward identification, yet a potentially complex system.

LOCK850.52: An extended counterpart at 24 μm, barely visible in the high-resolution radio image and yet obvious and extended in the lower-resolution map; extra resolution available in the LH has clearly hindered the identification process. The optical counterpart must be part of an extensive system, presumably largely obscured.

LOCK850.53: A typical counterpart consisting of two optical galaxies, betrayed by their 24-μm emission.

LOCK850.60: Several plausible identifications at 24 μm, the closest of which just fails to qualify as a robust counterpart.

LOCK850.63: Another plausible AO target.

LOCK850.67: Optically faint SMG, blank at 1.4 GHz, given away by its 24-μm emission.

LOCK850.70: A classic optical pair betrayed at 24 μm and by weak radio emission.

LOCK850.77: As LOCK850.34: a pair of pairs.

LOCK850.79: Another SMG with several plausible identifications, though only one of these is statistically robust.

LOCK850.87: Optically invisible, yet bright at 24 μm and 1.4 GHz.

SXDF850.01: Optically invisible, yet bright at 1.4 GHz.

SXDF850.02: The radio morphology resembles the base of a wide-angle tail radio galaxy.

SXDF850.03: The radio emission is apparently associated with a bright, nearby galaxy, though the alignment is poor and lensing of a background SMG must be a possibility.

SXDF850.05: Seemingly a multi-component merger; sufficiently bright at 24 μm and 1.4 GHz to suggest it lies at relatively low redshift.

SXDF850.06: An immensely complex region with at least three radio-detected components. The brightest 24-μm identification is coincident with the radio source most distant from the SMG centroid.

SXDF850.07: An optically faint SMG in a complex region, betrayed by its 24-μm and 1.4-GHz emission.

SXDF850.08: A robust radio identification, offset by several arcsec from a plausible 24-μm counterpart.

SXDF850.10: It is plausible that the submm emission emanates from between the hotspots of a lobe-dominated radio galaxy.

SXDF850.11: An excellent, clearly identified target for AO-assisted study, exploiting the nearby star.

SXDF850.12: An distorted optical counterpart lies beneath very faint radio emission close to the SMG centroid.

SXDF850.14: Near-coincident, faint 24-μm and 1.4-GHz emission, though it would be tempting to target the distorted optical galaxy north of the *Spitzer* emission for spectroscopy.

SXDF850.16: Faint radio emission is offset from a seemingly distorted optical counterpart by ∼1 arcsec.

SXDF850.21: A local galaxy lies close to this SMG – VLA0077 in the catalogue of Simpson et al. (2006), at $z = 0.044$; this must be viewed as the most likely identification – a rare example of a nearby galaxy in a blank-sky submm survey.

SXDF850.23: As SXDF850.16.

SXDF850.24: Two robust radio identifications, one near-coincident with faint 24-μm emission.

SXDF850.28: An immensely complex region with at least three radio-detected components, each with different 24-μm properties.

SXDF850.29: A bright radio identification – VLA0225 in the catalogue of Simpson et al. (2006) – offset significantly from the centroid of a bright $z = 0.264$ optical galaxy. The correct identification becomes obvious in the near-IR (Clements et al., in preparation).

SXDF850.30: This SMG is betrayed by 24-μm and 1.4-GHz emission; a nearby optical galaxy may be the unobscured component of a larger system.

SXDF850.31: Two robust 24-μm identifications, one coincident with radio emission, both with bright optical counterparts.

SXDF850.37: Optically faint SMG with near-coincident 24-μm and 1.4-GHz emission.

SXDF850.47: A complex region with three radio-detected components, each with near-coincident 24-μm emission.

SXDF850.52: Two robust radio identifications with very different optical properties, one bright, one invisible; the brightest of the optical galaxies is not well aligned with its radio emission.

SXDF850.77: A complex SMG with two radio emitters, neither of which is aligned well with the two 24-μm emitters in the region.

SXDF850.119: Two plausible identifications, each with very different optical properties – one bright and presumably relatively local; the other optically invisible, likely at high redshift.

APPENDIX B: POSITION AND FLUX ERRORS

Uncorrelated noise

Much of the theory needed for an understanding of SCUBA position errors can be found in Condon (1997), which treats the general case of fitting a Gaussian ellipsoid to map data, for which there are six free parameters: source coordinates, total flux, two principal axes and a position angle. For the present application, we generally prefer to assume that SCUBA sources will not be resolved by the beam, although resolved or blended sources are certainly known (Ivison et al. 2000; Stevens et al. 2003; Pope et al. 2005). The map should therefore consist of a scaled and shifted replica of the beam, plus noise. This leaves just three free parameters.

We follow Condon and assume that the beam is a single 2D Gaussian with an r.m.s. 'width' σ ($\simeq$ FWHM/2.354) in each coordinate. Let the coordinates of the centroid be (α, δ) and assume that the map is digitised on a (fine) grid where the pixel spacing is h and the noise value at each pixel is an independent zero-mean Gaussian deviate with r.m.s. value, μ; the units of μ are those of surface brightness. The peak value of the fitted profile is A; strictly, this is a surface brightness value and the total integrated flux density will be $S = 2\pi\sigma^2 A$. However, normally the factor $2\pi\sigma^2$ will be absorbed into map units of mJy beam^{-1} or equivalent, so that A has the numerical value of the flux density of a fitted unresolved source. With this notation, Condon's solution for the r.m.s. errors (Δ) on the three-parameter fit is

$$\Delta A = \sqrt{\frac{1}{\pi}} \frac{h}{\sigma} \mu$$
$$\Delta\alpha = \Delta\delta = \sqrt{\frac{2}{\pi}} \frac{\mu}{A} h. \tag{B1}$$

For a practical formula, it makes sense to combine these by defining the flux signal-to-noise ratio: SNR = $A/\Delta A$:

$$\Delta\alpha = \Delta\delta = \sqrt{2}\,(\text{SNR})^{-1}\,\sigma \simeq 0.6\,(\text{SNR})^{-1}\,\text{FWHM}. \tag{B2}$$

This is independent of h, as makes intuitive sense (although the derivation assumes $h \ll \sigma$). Note that Condon quotes a larger error in A for the 6-parameter case: this appears to be an error, but is in any case irrelevant for the present purpose.

Correlated noise and optimal filtering

A more serious problem with this result is that often the noise is not independent from pixel to pixel. This may be inherent in the data (e.g. interferometry maps, where the noise has the same coherence structure as a point source), or may be a result of smoothing the map. Smoothing may arise either via some form of 'drizzling' in the data reduction software, or can be an explicit convolution. The prime example of the latter is 'optimal filtering' in which the map is convolved again with the beam in an attempt to improve the visibility of true sources in comparison with the noise. This was the strategy used by Scott et al. (2002) to identify candidate sources for detailed fitting to the unsmoothed data. In this case there is no fitting of the position of the source: the position is taken as the location of a peak in the filtered map.

A slightly more general problem is now to consider a 'source' in the form of a Gaussian of height B and width σ_s superimposed on a correlated noise field $n(\alpha)$ produced by smoothing white noise with a Gaussian of width σ. The resulting noise field will have an r.m.s. value ϵ and we are interested in both SNR = B/ϵ and the
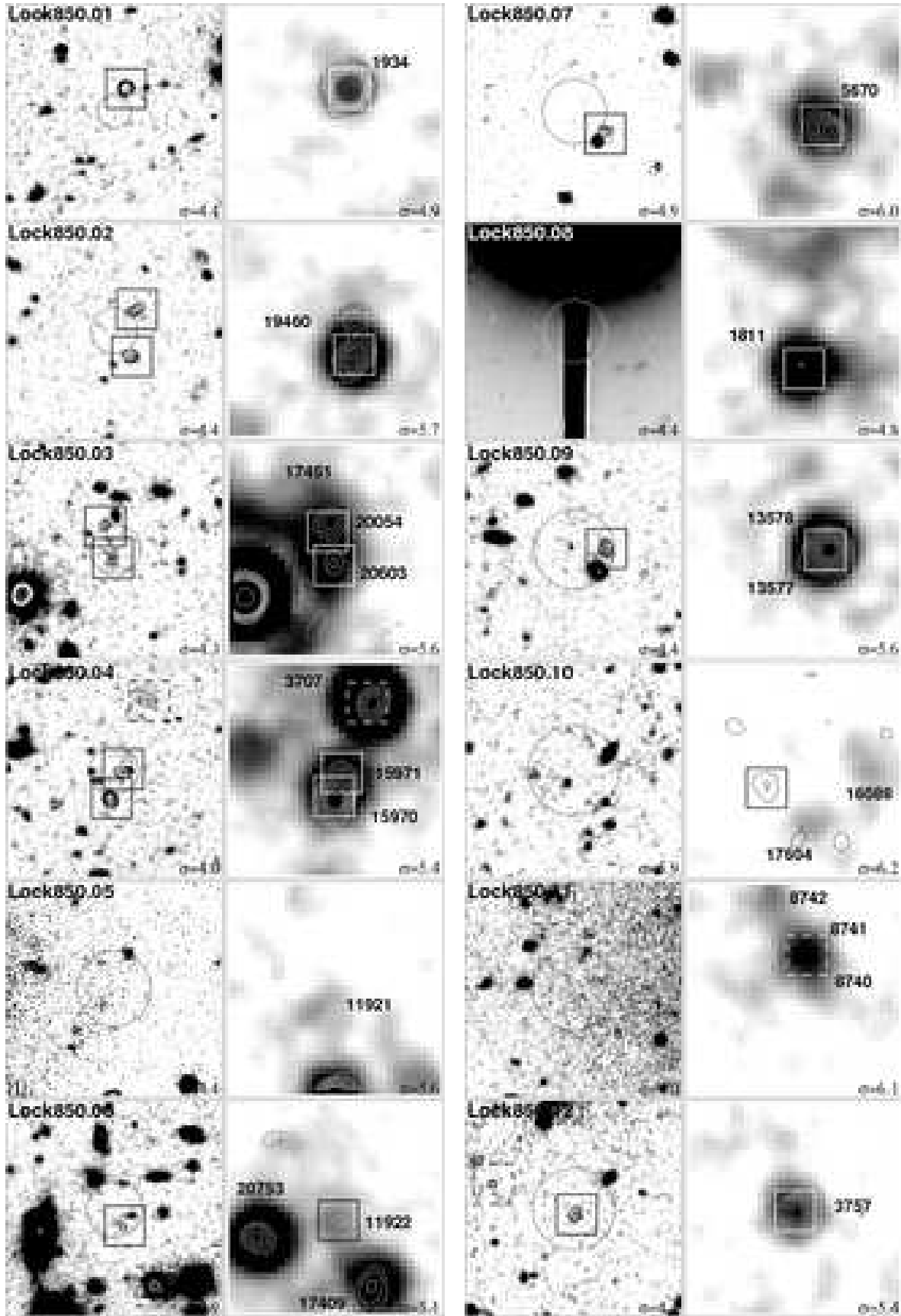
Figure A1. 25 × 25-arcsec postage stamp images of each SMG in the LH SHADES Source Catalogue. Greyscale R-band and 24-μm data are shown in the left- and right-hand panels, respectively, superimposed with radio contours. Circles indicate 2σ positional uncertainties. Solid boxes indicate robust identifications, where $P \leqslant 0.05$ based on the radio or 24-μm counts, or a combination of the two. Dashed boxes indicate tentative associations.
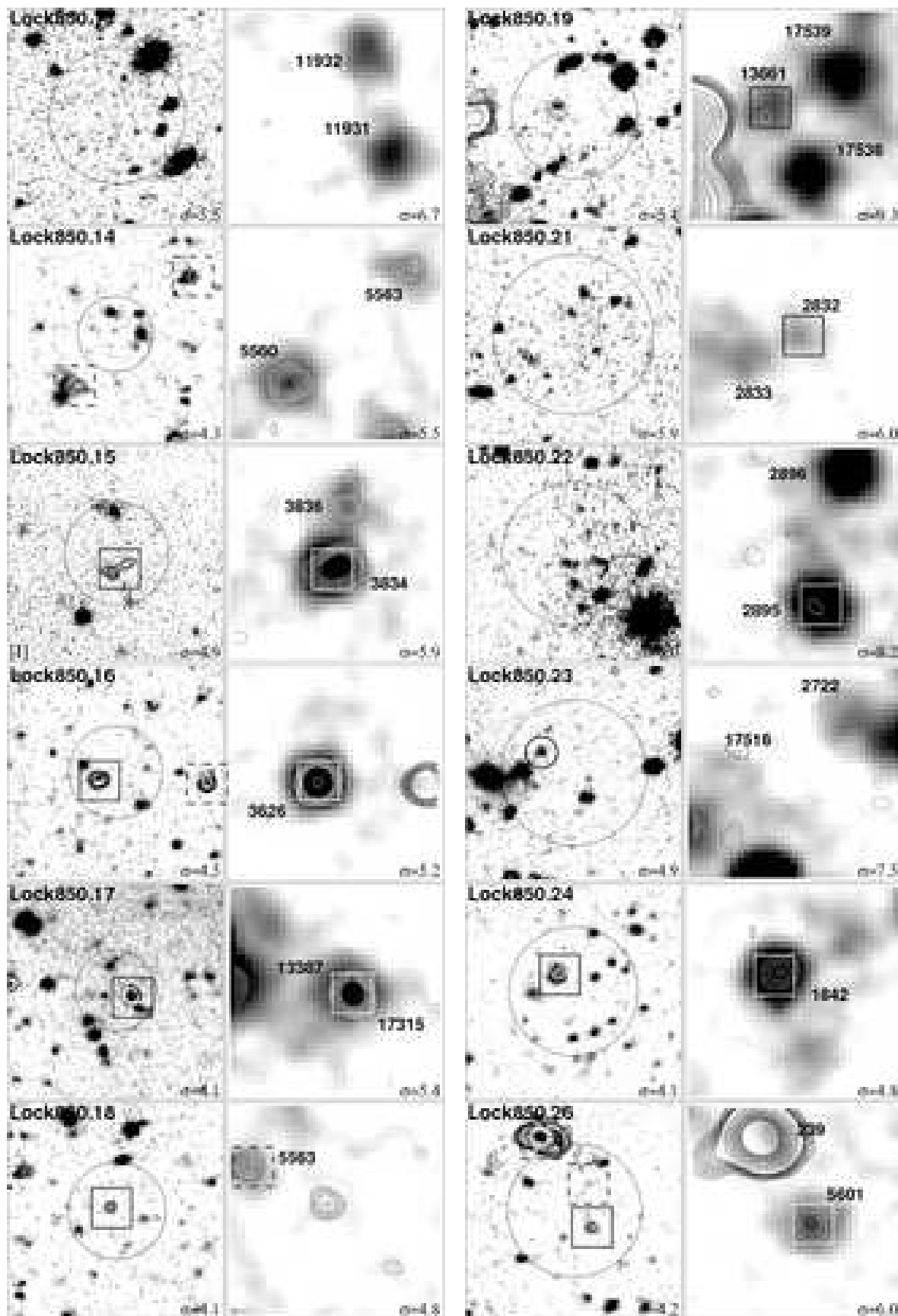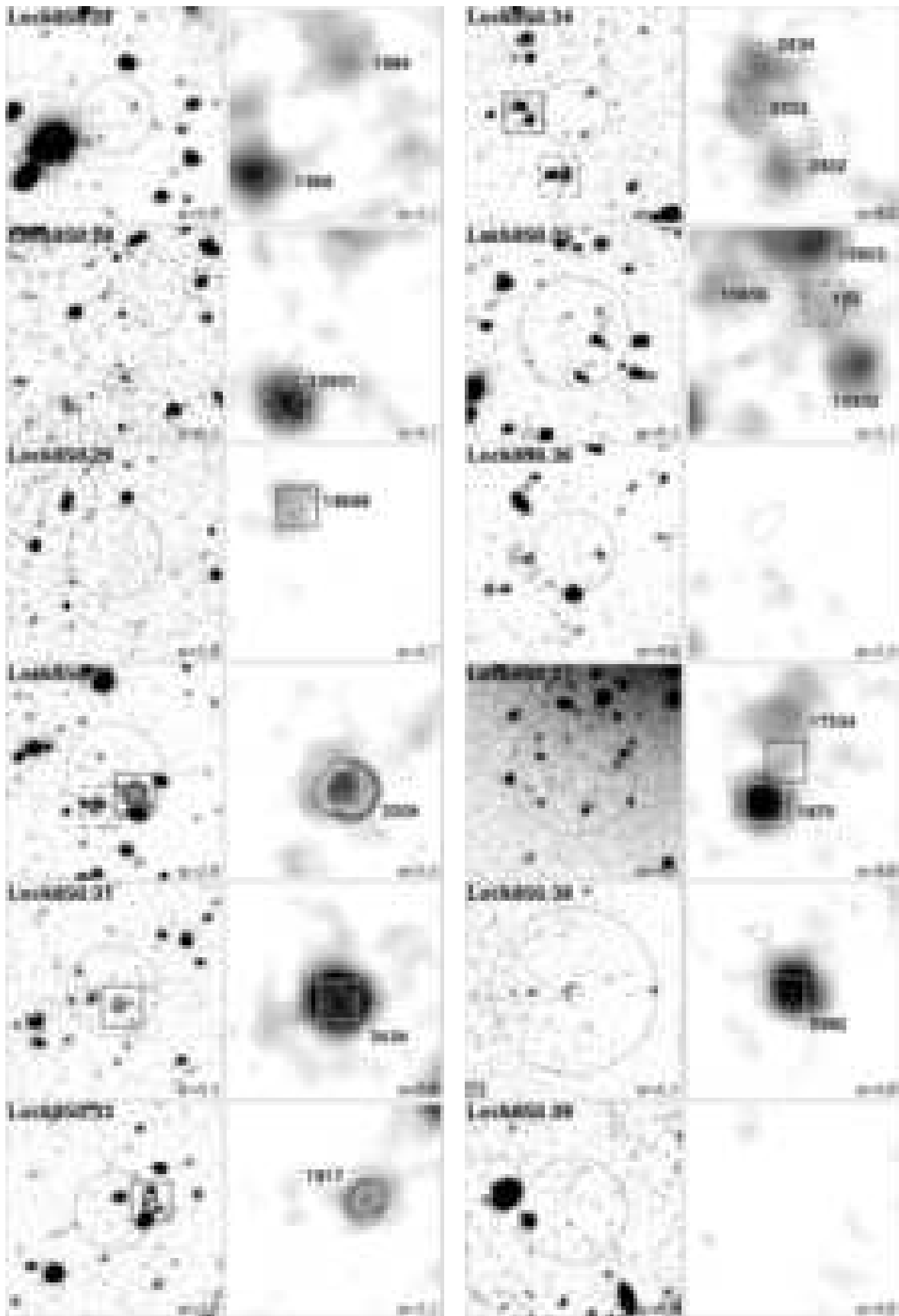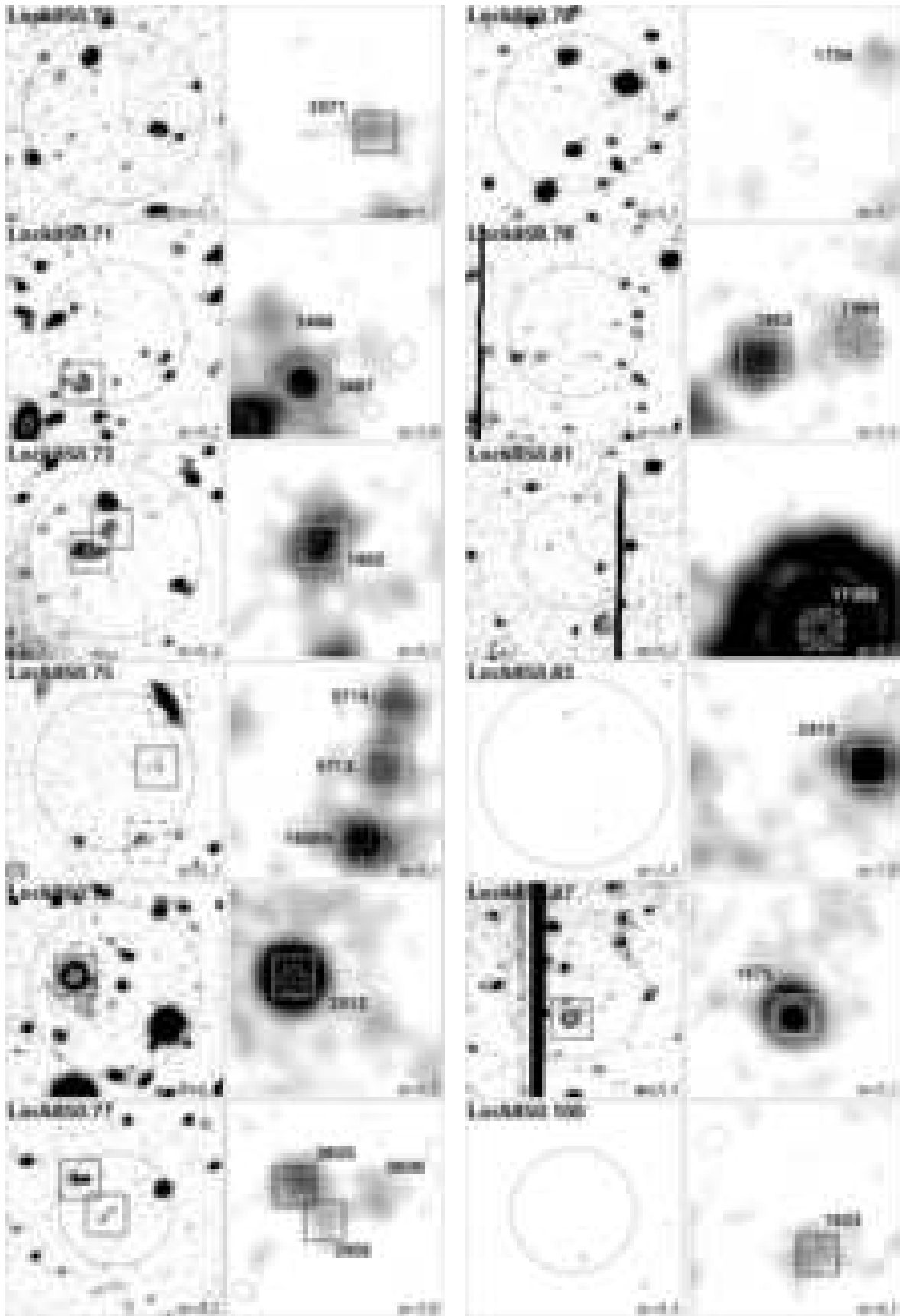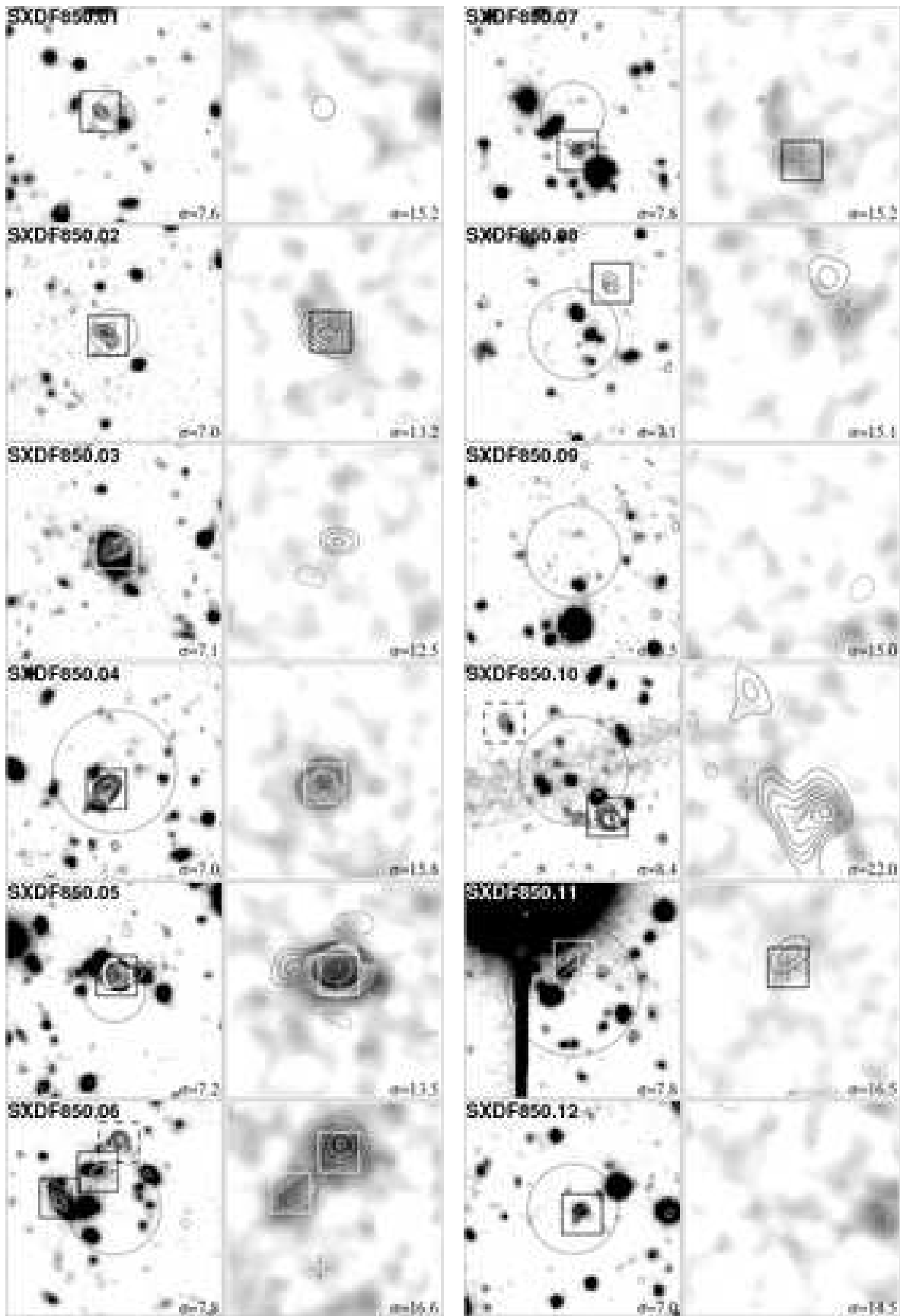
Figure A1. Cont...

**Figure A1.** Cont...
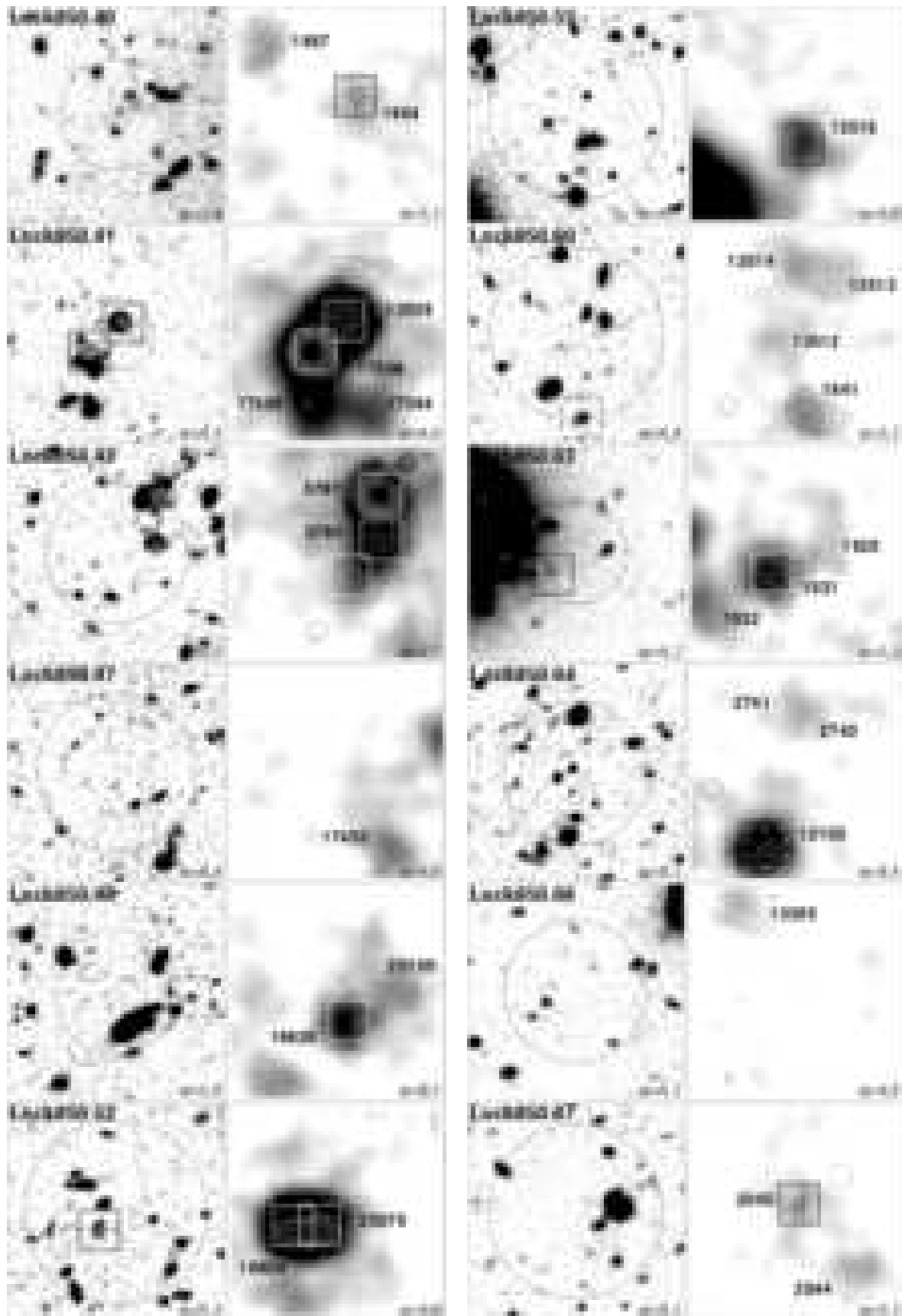
Figure A1. Cont...

Figure A1. Cont...

Figure A2. 25 × 25-arcsec postage stamp images of each SMG in the SXDF SHADES Source Catalogue. Greyscale *R*-band and 24-μm data are shown in the left- and right-hand panels, respectively, superimposed with radio contours. Circles indicate 2σ positional uncertainties. Broken crosses mark 24-μm sources brighter than 150 μJy within 15 arcsec of SMG positions – their positions are listed in Table 4. Solid boxes indicate robust identifications, where $P \leqslant 0.05$ based on the radio or 24-μm counts, or a combination of the two. Dashed boxes indicate tentative associations.
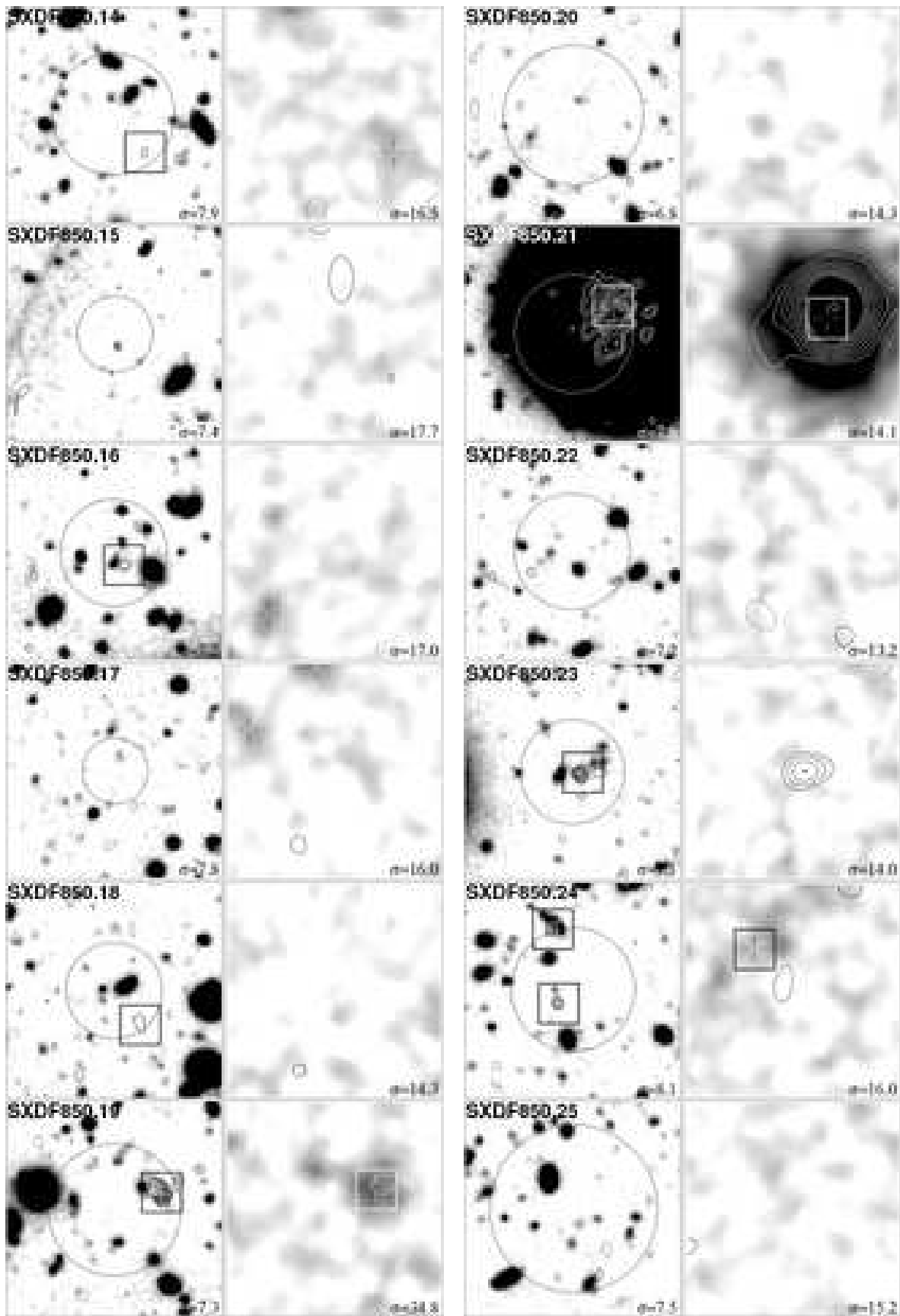
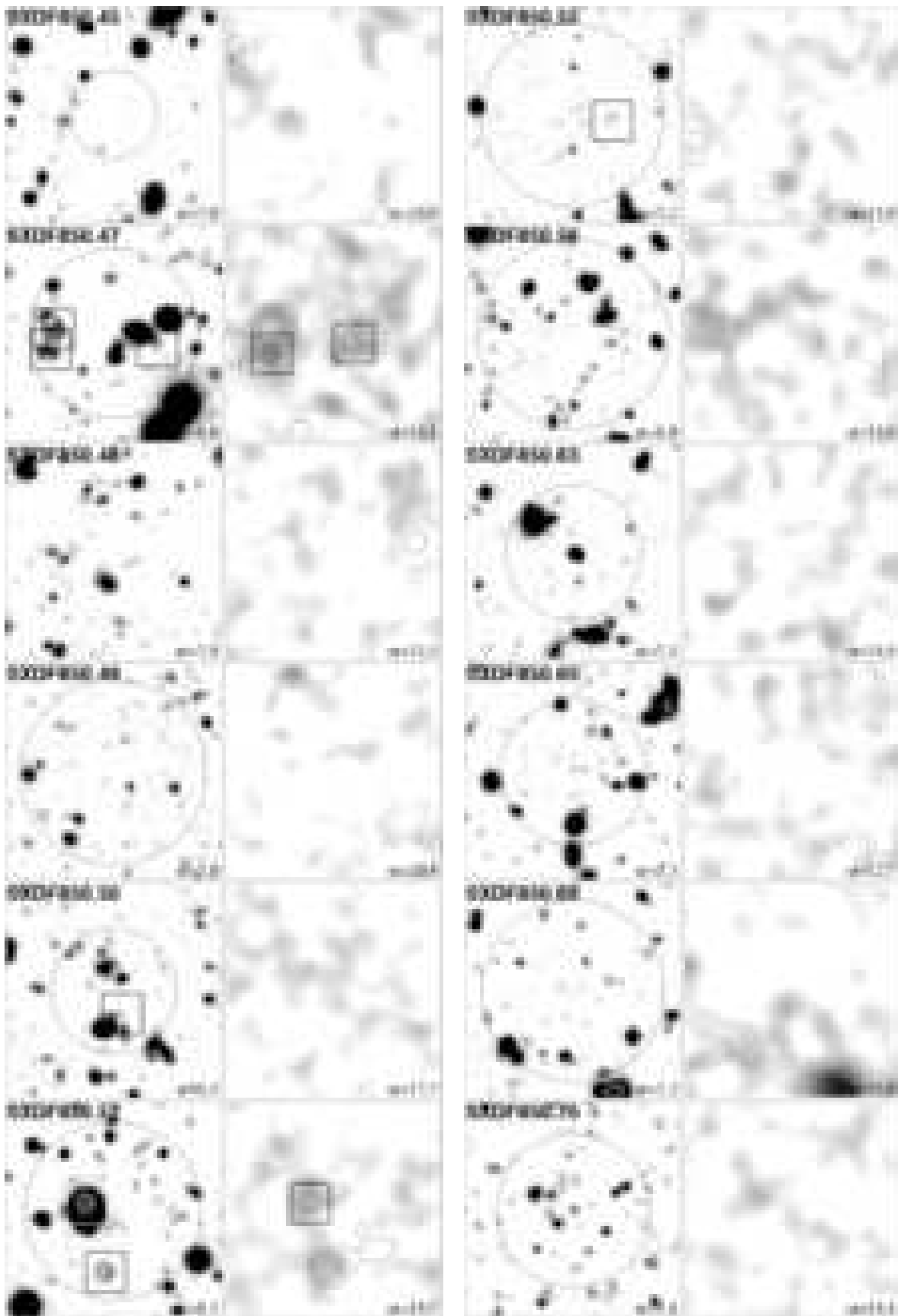**Figure A2.** Cont...
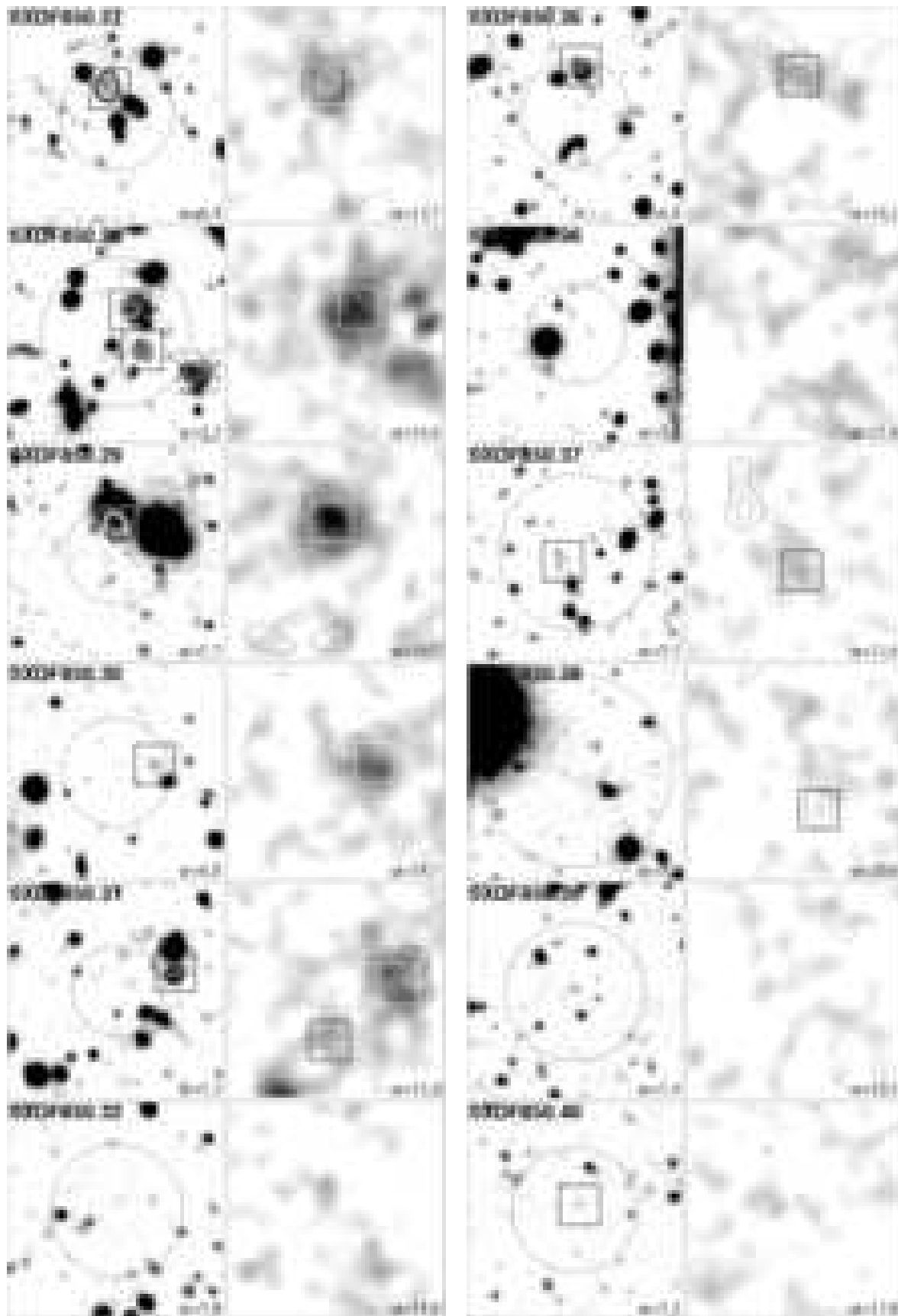
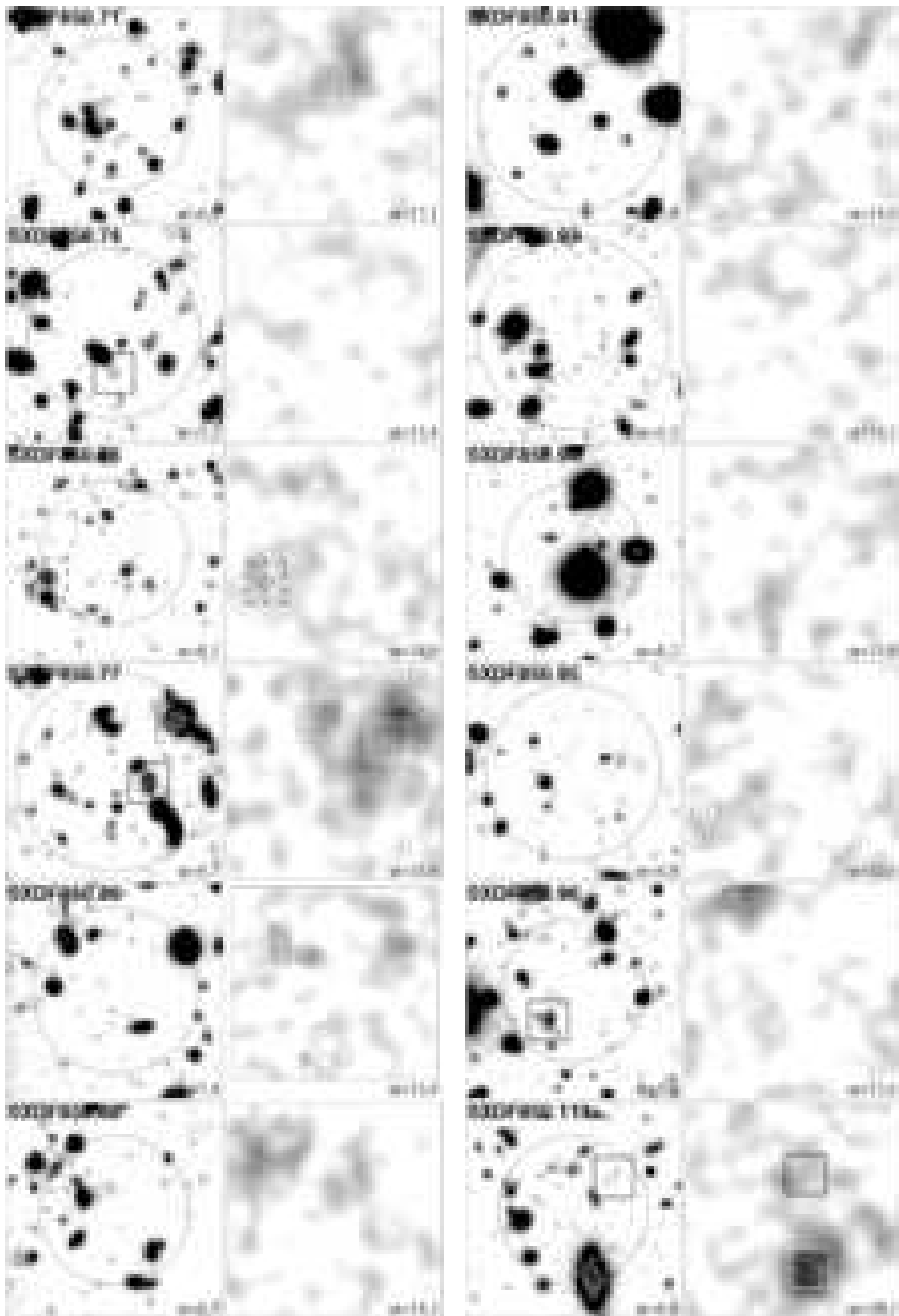**Figure A2.** Cont...

Figure A2. Cont...

Figure A2. Cont...

error in the position of the peak. The latter can be solved by considering a Taylor expansion of the signal S around the peak (in one coordinate, x, and assuming the true source to be centred at $x = 0$):

$$S(\alpha) \simeq B(1 - x^2/2\sigma_s^2) + n + n'x + n''x^2/2, \qquad (B3)$$

where n' denotes dn/dx, etc. For large B, the last term is negligible, so the apparent position of the peak is just $x = \sigma_s^2 n'/B$. The r.m.s. positional errors in each coordinate are then

$$\Delta\alpha = \Delta\delta = \frac{\sigma_s^2}{B} \left\langle (n')^2 \right\rangle^{1/2}. \qquad (B4)$$

The r.m.s. value of the gradient in Gaussian-filtered white noise is straightforward to evaluate (e.g. using equations 16.41 and 16.42 of Peacock 1999):

$$\left\langle (n')^2 \right\rangle = \frac{\langle n^2 \rangle}{2\sigma^2} = \frac{\epsilon^2}{2\sigma^2}. \qquad (B5)$$

In terms of $\mathrm{SNR} = B/\epsilon$, this gives

$$\Delta\alpha = \Delta\delta = 2^{-1/2} \frac{\sigma_s}{\sigma} (\mathrm{SNR})^{-1} \sigma_s. \qquad (B6)$$

The appropriate value of σ_s depends on the application. For interferometry data, $\sigma_s = \sigma$, so we have

$$\Delta\alpha = \Delta\delta = 2^{-1/2} (\mathrm{SNR})^{-1} \sigma \simeq 0.3\,(\mathrm{SNR})^{-1}\,\mathrm{FWHM}. \quad (B7)$$

For the case of optimal filtering, the source is broadened so that $\sigma_s = \sqrt{2}\,\sigma$, yielding

$$\Delta\alpha = \Delta\delta = \sqrt{2}\,(\mathrm{SNR})^{-1} \sigma \simeq 0.6\,(\mathrm{SNR})^{-1}\,\mathrm{FWHM}. \qquad (B8)$$

This is of the identical form to the result for the gridded data. However, the definitions of SNR are different in the two cases; to finish, we need to prove that they are, in practice, identical.

First, suppose we allow ourselves any filtering scale, σ_f. The filtered source width satisfies $\sigma_s^2 = \sigma^2 + \sigma_f^2$ and flux conservation gives $B = A(\sigma/\sigma_s)^2$. The r.m.s. of the filtered white noise can be worked out most simply by Fourier transforming the original noise field, multiplying by the transform of a Gaussian filter and squaring to get the new noise power spectrum, which is then integrated to get the new noise variance. The unfiltered noise variance is derived by considering a constant power spectrum over the Nyquist range of wavenumbers between $-\pi/h$ and $+\pi/h$. The filtered result can then be expressed as

$$\epsilon = \frac{h}{\sqrt{4\pi}\,\sigma_f}\,\mu \qquad (B9)$$

(provided $\sigma_f \gg h$), so the SNR of the filtered peak is

$$\mathrm{SNR}_{\mathrm{peak}} = \frac{\sqrt{4\pi}\,A\sigma^2 \sigma_f}{\mu h \sigma_s^2}. \qquad (B10)$$

This has a maximum at $\sigma_f = \sigma$, verifying the optimal filter result and giving

$$\mathrm{SNR}_{\mathrm{peak}} = \frac{\sqrt{\pi}\,A\sigma}{\mu h}, \qquad (B11)$$

which is identical to Condon's result (eqn 1). Thus, we have verified that optimal filtering returns the same SNR as direct fitting to the pixel data, and shown that it also yields identical positional errors.

Correction for flux boosting

It is well known that a flux-limited sample selected in the presence of noisy fluxes suffers two related effects: too many sources are found (Eddington bias) and the selected sources have their fluxes

systematically over-estimated. This is sometimes loosely called Malmquist bias although, strictly speaking, Malmquist bias is the effect on the mean flux of a distribution due to the imposition of a flux limit. A Malmquist bias persists even without noise. A more prosaic term for the latter effect is 'flux boosting'; in practice the observed SNR values for SCUBA sources will thus be too high. The standard form for the Malmquist correction (see e.g. §3.6.1 of Binney & Merrifield 1998) in magnitude units is

$$\Delta m = -\sigma^2 \frac{d\ln(dN/dm)}{dm}, \qquad (B12)$$

where dN/dm is the differential number counts and here σ means the r.m.s. magnitude error. We shall assume power-law counts with $N(>f) \propto f^{-\beta}$, so that $\Delta m = -0.4\beta \ln 10\,\sigma^2$, and the apparent SNR from the Malmquist formula is

$$\mathrm{SNR}_{\mathrm{app}} = \mathrm{SNR}\,\exp(\beta/\mathrm{SNR}^2). \qquad (B13)$$

However, the Binney & Merrifield formula does not apply in this case, because the measurements are subject to flux errors, rather than the magnitude errors assumed in their approach. It is straightforward to derive the appropriate correction by taking a Bayesian approach, as has also been followed in Coppin et al. (2005). If the apparent flux is f_a, we want to know the conditional distribution of the corresponding true flux, f, which is

$$P(f|f_a) \propto P(f)\,P(f_a|f). \qquad (B14)$$

The prior, $P(f)$ is just the (power-law) number counts, and $P(f_a|f)$ is just the Gaussian error distribution $\propto \exp[-(f_a - f)^2/2]$ (we implicitly set the r.m.s. noise equal to unity, so as to work in SNR units). This equation has the drawback that $P(f|f_a)$ diverges at $f = 0$, reflecting the fact that the confusion limit has not been allowed for, but there is a well-defined maximum is the conditional distribution, and we take this as the best estimate of f given f_a. This is easily shown to be

$$f = f_a/2 + \sqrt{f_a^2/4 - (\beta+1)}. \qquad (B15)$$

Before adopting this as a correction for flux boosting, however, there is one further correction to consider, which increases the size of the effect. This arises because we have assumed implicitly that the location of the source is known, so that the apparent flux is the true flux plus a noise term. But we have shown above that the existence of a noise field inevitably introduces position errors, so that we are never measuring exactly at the true position of the source. The effect of position errors on the apparent flux is easy to analyse, following our earlier formulae. The variation in signal with one coordinate, x, around a peak is approximately

$$S(x) \simeq f(1 - x^2/2\sigma_s^2) + n + n'x, \qquad (B16)$$

and we have already shown the effect of the noise gradient n' in perturbing the position of the peak. But it also perturbs the *height* of the peak, which is the apparent flux:

$$f_a = f + n + (n'\sigma_s)^2/2f. \qquad (B17)$$

For Gaussian noise, the gradient n' is independent of the amplitude of the noise, n, so there is an additional boost of the flux – which is largest for those sources with the largest positional errors. In terms of the offset in one coordinate, Δx, the flux boost is

$$\Delta f/f = (\Delta x)^2/2\sigma_s^2. \qquad (B18)$$

There is an independent effect from each coordinate, so that the expected size of the boost from gradients is

$$\langle \Delta f \rangle = \langle (n')^2 \rangle \sigma_{\rm s}^2 / f = \epsilon^2 \sigma_{\rm s}^2 / 2f\sigma^2, \tag{B19}$$

using our previous expression for the r.m.s. gradient. We will ignore the dispersion in this correction, since it is usually much smaller than the dispersion in n. Since the noise field and the noise gradient are independent, we can correct for them in turn. If we take out previous deboosted estimate, f, the correction for gradient bias to yield the final estimate of the true flux, f_t, is

$$f_t = f/2 + \sqrt{f^2/4 - 1} \tag{B20}$$

(where we have assumed optimal filtering, so $\sigma_{\rm s}^2 = 2\sigma^2$).

Combining these two steps yields a cumbersome expression for the true SNR in terms of the apparent SNR, and we advocate the following convenient approximation as suitable for use when the apparent SNR exceeds 3:

$$\mathrm{SNR} = \sqrt{\mathrm{SNR}_{\mathrm{app}}^2 - (2\beta + 4)}. \tag{B21}$$

Our final suggested formula for the expected position errors is thus

$$\Delta\alpha = \Delta\delta = 0.6 \left[\mathrm{SNR}_{\mathrm{app}}^2 - (2\beta + 4)\right]^{-1/2} \mathrm{FWHM}. \tag{B22}$$

Strategy for optimal source reliability

It may seem self-evident that optimal filtering as discussed above is also the best strategy for source detection (neglecting confusion) – but this is not so obvious. Optimal filtering gives the most accurate measurement of the flux for a given source. For detection, we want to minimise the probability of noise alone yielding a spurious source of the observed height. If we smooth an image with a filter that is broader than optimal, the apparent SNR goes down – but nevertheless the expected number of noise peaks on the image of this new height may go down, just because of the larger coherence length in the new noise field.

This all works out quite simply for Gaussian filtering and a Gaussian source: the apparent SNR ($\equiv \chi$) is

$$\chi = \mathrm{SNR} \, 2\xi/(1 + \xi^2), \tag{B23}$$

where $\xi = \theta_{\mathrm{filter}}/\theta_{\mathrm{beam}}$ and SNR means the standard optimally-filtered value. The number density of peaks with height above χ is proportional to $N = \xi^{-2}\chi \exp(-\chi^2/2)$ (for $\chi \gtrsim 3$; see Bond & Efstathiou 1987). So, we need to vary ξ to minimise N. As a function of the optimally-filtered SNR, the numerical value of the required ξ can be approximated empirically by

$$\xi \simeq 1 + 2/\mathrm{SNR}^2. \tag{B24}$$

Thus, for our typical 4-σ threshold, we should in principle filter with something about 15 per cent broader than the beam to give us the best chance that the sources are real. This is not a big effect and we have chosen to ignore it, but it is an interesting point of principle.